Accepted Manuscript

A DEM model for visualising damage evolution and predicting failure envelope of composite laminae under biaxial loads

Yaser Ismail, Dongmin Yang, Jianqiao Ye

PII: S1359-8368(16)30086-5

DOI: 10.1016/j.compositesb.2016.07.004

Reference: JCOMB 4433

To appear in: *Composites Part B*

Received Date: 21 March 2016

Revised Date: 11 June 2016

Accepted Date: 4 July 2016

Please cite this article as: Ismail Y, Yang D, Ye J, A DEM model for visualising damage evolution and predicting failure envelope of composite laminae under biaxial loads, *Composites Part B* (2016), doi: 10.1016/j.compositesb.2016.07.004.

A DEM model for visualising damage evolution and predicting failure envelope of composite laminae under biaxial loads

Yaser Ismail[a], Dongmin Yang[b,*], Jianqiao Ye[a,†]

[a] Department of Engineering, Lancaster University, Lancaster LA1 4YR, UK

[b] School of Civil Engineering, University of Leeds, Leeds LS2 9JT, UK

Abstract

A two dimensional particle model based on the discrete element method (DEM) is developed for micromechanical modelling of fibre reinforced polymer (FRP) composite laminae under biaxial transverse loads. Random fibre distribution within a representative volume element (RVE) is considered for the micromechanical DEM simulations. In addition to predicting the stress-strain curves of the RVEs subjected to transverse compression and transverse shear stresses against the experimental testing results and other numerical modelling results, the DEM model is also able to capture the initiation and propagation of all micro damage events. Fibre distribution is found to more significantly influence the ultimate failure of composite laminae under transverse shear, while it has much less effect on the failure under transverse compression. The failure envelope of composite laminae under biaxial transverse compression and transverse shear is predicted and compared with Hashin and Puck failure criteria, showing a reasonable agreement. The predicted failure envelope is correlated with the damage evolution and the quantitative analysis of failure events, which improves the understanding of the failure mechanisms.

Key words: FRP; damage evolution; failure criterion; DEM; micromechanical modelling.

1. Introduction

Fibre reinforced polymer (FRP) composite laminates have been widely used over the past thirty years in aerospace industries mainly due to their high stiffness-weight and strength-weight ratios. However, there is yet a universal model or approach to accurately predict the failure strength of FRP composite laminates under biaxial or triaxial loads in real applications [1]. A large amount of experimental tests need to be carried out to obtain the failure strength of FRP composite laminates which is usually designed to be much larger than the required strength under real loading conditions. This means that in many cases the FRP composites are over safely designed and their advantages of light weight and design flexibility have not been maximised. In addition, the experimental tests are affected by the testing environment and the results are very diverse, especially when materials are subjected to a system of loads including transverse load that is very difficult to carry out. Therefore, an accurate and

*Corresponding author 1. Email: d.yang@leeds.ac.uk

†Corresponding author 2. Email: j.ye2@lancaster.ac.uk

universal approach for predicting the strength of FRP composite laminates is always highly demanded.

Generally, five different failure mechanisms could occur in composite laminates and they depend mainly on the loading conditions and directions [2]. Fibre fracture and localised fibre buckling occur when tension and compression are, respectively, applied along the fibre direction. Tensile load applied in the direction perpendicular to the fibres results in either fibre/matrix debonding or matrix cracking. Delamination takes place between plies and has to be considered in order to predict the laminate behaviour precisely. There are a few theoretical failure criteria available for predicting failure modes separately as well as the failure envelope of composite lamina/laminates under different loading conditions. Among them, there are several well-known physically-based phenomenological failure criteria [3-6] that have the capability to predict the failure envelope and also provide information on failure modes of composite lamina/laminates under certain loading conditions [1]. In particular, Puck's failure criterion is one of the better criteria adopted in the World Wide Failure Exercise (WWFE) for predicting composite laminate failure. However, these criteria contain several non-physical parameters that need to be obtained from specific and challenging experimental tests. It has been shown in WWFE that the predictions of failure strength under some loading conditions (in particular biaxial and triaxial loads) by existing failure criteria are not accurate enough. One of the main reasons is that these criteria have not considered the effects of heterogeneous material microstructure and the interaction as well as progression between different failure modes. Theoretically it is not straightforward to dynamically correlate different failure modes during the failure process as the random and heterogeneous microstructure of composite lamina/laminates are hardly to be considered. Micromechanics analysis is very useful for studying the mechanical behaviour of FRP composite laminates and understanding their damage process and failure strength. Within the framework of micromechanical modelling, the macroscopic properties are obtained through a representative volume element (RVE) of the material microstructure. Unlike the conventional homogenisation techniques, micromechanical modelling can take into account the details of geometry and fibre distribution to compute the stresses and strains in each material constituents, which leads to more accurate predictions of damage initiation and propagation and failure strength [7].

Two different approaches have been widely employed for numerical micromechanical modelling. The first approach assumes that the fibres are periodically distributed and uses a unit cell consisting of one or two fibres for the modelling. For example, Paris *et al.*, [8] used a single fibre unit cell to study the fibre/matrix debonding of a glass-epoxy composite. Ha *et al.*, [9] determined the failure envelope of a composite lamina under biaxial loads by modelling a unit cells of square and hexagonal fibre arrangements. The second approach uses a RVE in which several dozens of fibres are distributed randomly. Intensive studies have been carried out using this method to understand the effects of RVE size, position of fibres and internal distance between fibres on the elastic properties as well as the strength of FRP composite laminae. For instance, Trias *et al.*, [10] concluded that the minimum size of carbon fibre reinforced polymer with a volume fraction of 50% is $\delta = L/r_f = 50$, where L is the side of the RVE and r_f is the fibre radius. Yang [11] found that inter-fibre spacing has a significant impact on the transverse tensile and compressive strength of composites, especially when thermal residual stress is taken into account.

Apart from FEM modelling, discrete element method (DEM) has been recently introduced to model the damage evolution in composites. For instance, the crack propagation and stress-strain curves of composite materials under transverse tensile loading was simulated by DEM in [12, 13]. It was concluded that DEM has advantages of tracing the crack path within the microstructures in addition to predicting the final failure strength. Yang *et al*., [14, 15] also investigated the transverse cracks and delamination in cross-ply laminates and predicted the crack density using two dimensional DEM. With the increasing of computer power and the lowering of the cost, DEM has become more beneficial than traditional numerical approaches in studying damage initiation and crack propagation at microscopic scale. For instance, Maheo *et al*., [16] used three dimensional DEM to model the damage of a composite material under uniaxial tension. Although the model assumed a periodic distribution of fibres and used only one fibre, it has demonstrated the potential of DEM for modelling the failure process as well as failure strength under real uniaxial loads in three dimensions.

Despite of the massive research efforts recently devoted to investigating the failure behaviour of composite laminates under shear loading [17-22], the damage mechanisms and failure theory are still not fully understood. Therefore this paper aims to extend our previous work on DEM modelling of composite materials from uniaxial loading to biaxial loading. Two dimensional DEM is used to visualise the damage mechanisms and to predict the stress-strain curves as well failure strength of composite lamina under three different types of loads, *i.e*., transverse compression, transverse shear and biaxial loads. The stress-strain curves obtained in this paper have advantages over those from traditional numerical models as the microscopic damage at different loading levels can be clearly visualised. The failure envelope of MY750 matrix reinforced by E-glass fibres under both transverse normal and shear loads is also predicted by DEM and compared with Puck [5] and Hashin [3] failure criteria.

2. The discrete element method (DEM) and its contact models

In two dimensional DEM, circular elements (or particles) are used to discretise the material domain, as shown in Fig.1. Each particle in DEM has mass and its motion is governed by the Newton's Second Law. The particles can be rigid or deformable, and interact with each other through contacts. To represent the mechanical behaviour of a bulk material, a bonding model is usually employed to bond two rigid particles at the contact. A few bonding models have been reported in literatures to numerically achieve the desired material properties. For instance, André *et al*., [23] developed a cohesive beam model which later was used by [16] to predict the damage of a composite material. In this study, however, the parallel bond model developed in [24] is adopted. The parallel bond can be described as a finite-sized piece of cementitious material deposited between two contacting particles, and can be envisioned as a set of elastic springs uniformly distributed over its cross-section. When two particles are bonded by a parallel bond the overall behaviour the contact is a result of particle-particle overlap (grain-based part) and parallel bond (cement-based part), as shown in Fig.1.

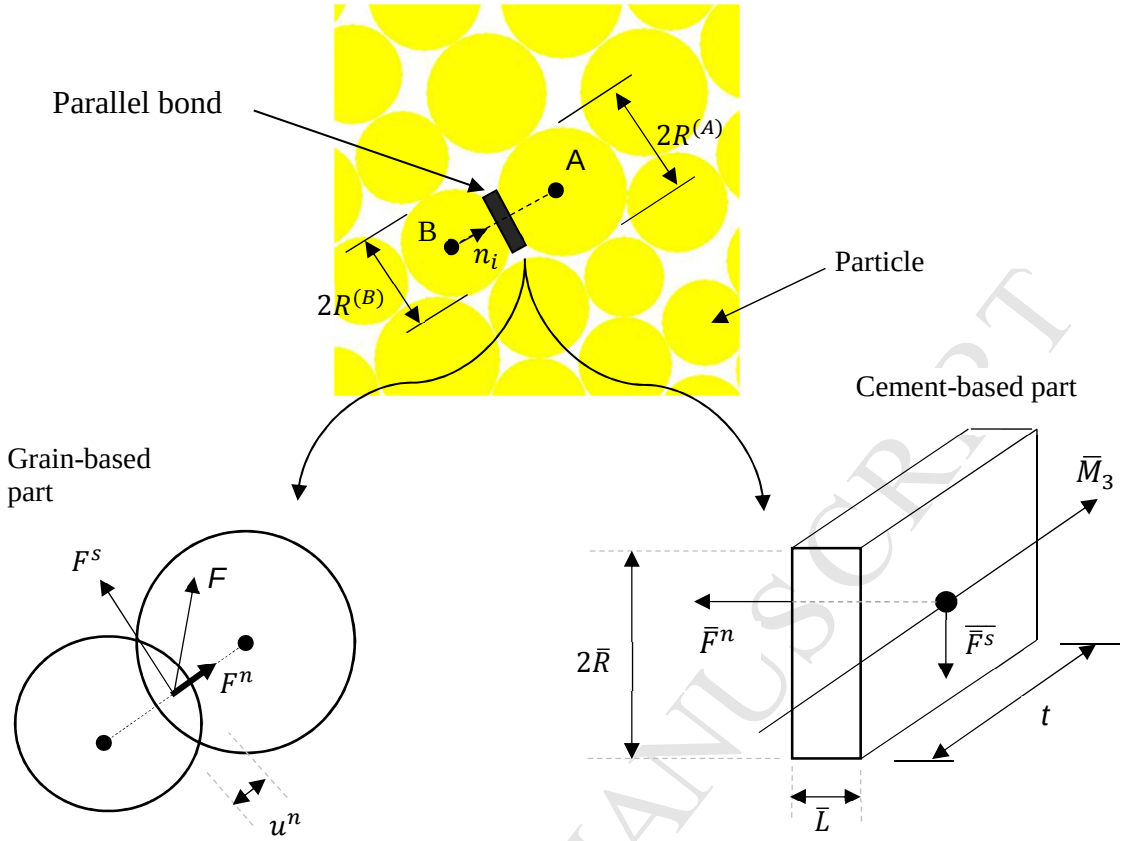

Fig.1 Schematic diagram of the parallel bond.

The grain-based part is represented by a linear contact model that can be described as a pair of springs at the contact (one in the normal direction and the other one in the shear direction). The inter-particle force, *F*, acting at the contact point represents the action between elements *A* and *B* and may be decomposed into a normal force F^n and a shear force F^s. These forces are related to the relative displacements through normal and shear stiffness k^n and k^s as follows:

$$F^n = k^n u^n \tag{1}$$
$$\Delta F^s = -k^s \Delta u^s \tag{2}$$

where u^n and Δu^s are the overlap and incremental tangential displacement, respectively; *k* is the resultant contact stiffness calculated by:

$$k^n = \frac{k_n^{(A)} k_n^{(B)}}{k_n^{(A)} + k_n^{(B)}} \tag{3}$$
$$k^s = \frac{k_s^{(A)} k_s^{(B)}}{k_s^{(A)} + k_s^{(B)}} \tag{4}$$

where $k_n^{(A)}$and$k_n^{(\boldsymbol{B})}$ are the normal stiffness, and $k_s^{(A)}$and $k_s^{(B)}$ are the shear stiffness of particles *A* and *B*, respectively.

The force $\bar{F}$ and moment $\bar{M}$ associated with cement-based part are calculated by:

$$\Delta\bar{F}^n = \bar{k}^n A \Delta u^n \quad (5)$$
$$\Delta\bar{F}^s = -\bar{k}^s A \Delta u^s \quad (6)$$
$$\Delta\bar{M} = -\bar{k}^n I \Delta\theta \quad (7)$$

Where $\bar{F}^n$ and $\bar{F}^s$ are axial and shear forces, respectively; θ is the rotation between two bonded particles; and A and I are the area and second moment of area of parallel bond cross section, respectively:

$$A = 2\bar{R}t \qquad (t = 1 \text{ in 2D}) \quad (8)$$
$$I = \frac{2}{3}\bar{R}^3 t \qquad (t = 1 \text{ in 2D}) \quad (9)$$

It is important to note, since parallel bonds act in parallel with the linear contact model, the overall stiffness at the contact K is:

$$K^n = (k^n) + \left(A\bar{k}^n\right) \quad (10)$$
$$K^s = (k^s) + \left(A\bar{k}^s\right) \quad (11)$$

The maximum tensile stress $\bar{\sigma}$ and shear stress $\bar{\tau}$ carried by the parallel periphery (cement-based part) are calculated by:

$$\bar{\sigma} = \frac{-\bar{F}^n}{A} + \frac{|\bar{M}|\bar{R}}{I} \quad (12)$$
$$\bar{\tau} = \frac{|\bar{F}^s|}{A} \quad (13)$$

If $\bar{\sigma} \geq \bar{\sigma}_c$ or $\bar{\tau} \geq \bar{\tau}_c$ the parallel bond breaks and a crack is generated. In this paper, the parallel bonds are used to model fibres and matrix. The mechanical properties of the bond will be calibrated against macro properties in the following section. The force-displacement laws for the normal and shear components of a parallel bond are shown in Fig.2. More details of DEM theory and parallel bond can be found in [24] and [25].

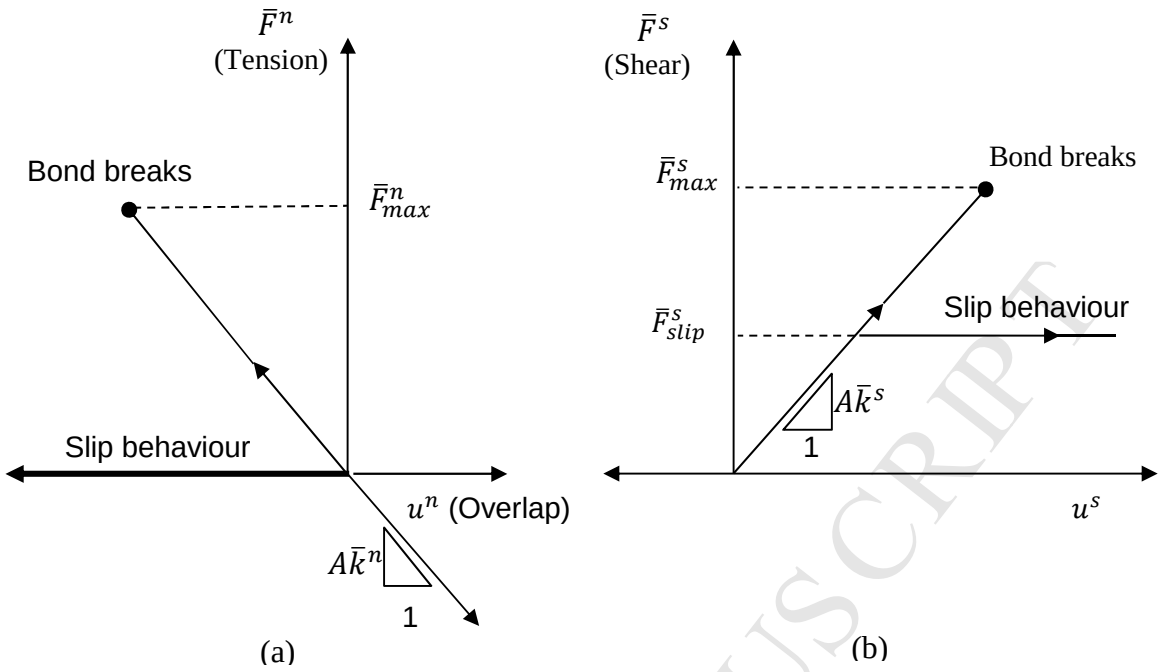

Fig.2 Force-displacement laws of parallel bond model: (a) normal behaviour, and (b) shear behaviour.

Debonding of fibre/matrix interface upon loading is accounted for by a contact softening model which is similar to the cohesive element used in FEM models. In contact softening model the strength is reduced as a linear function of the displacement after the peak strength, as shown in Fig.3. The initial response in absence of damage is linear elastic and the force increments, ΔF^n and ΔF^s, are calculated as a function of displacements, ΔU^n and ΔU^s:

$$\Delta F^n = K^n \Delta U^n \quad (n\text{: normal, } s\text{: shear}) \tag{12}$$

$$\Delta F^s = K^s \Delta U^s \tag{13}$$

The contact strength F_{max} is calculated from the two strength parameters (*i.e.*, F_c^n and F_c^s) and the current orientation of the contact force:

$$F_{max} = \left(1 - \frac{2\alpha}{\pi}\right) \cdot F_c^n + \frac{2\alpha}{\pi} \cdot F_c^s \tag{14}$$

where α is the angle between the directions of the contact force and the line segment connecting the centres of two contacted particles. The yielding of the bond in tension is determined by comparing the resultant contact force, *i.e.*,

$$F = \sqrt{(F^n)^2 + (F^s)^2} \tag{15}$$

with the contact strength. The contact yields if the contact force is larger than the contact strength:

$$F > F_{max} \tag{16}$$

When yielding occurs, the increment of contact displacements ΔU is the sum of elastic and plastic contact displacement increments:

$$\Delta U^n = \Delta U_e^n + \Delta U_p^n \quad (n\text{: normal, } s\text{: shear}) \tag{17}$$
$$\Delta U^s = \Delta U_e^s + \Delta U_p^s \tag{18}$$

More details of the contact softening model are discussed in [14, 15] and [25].

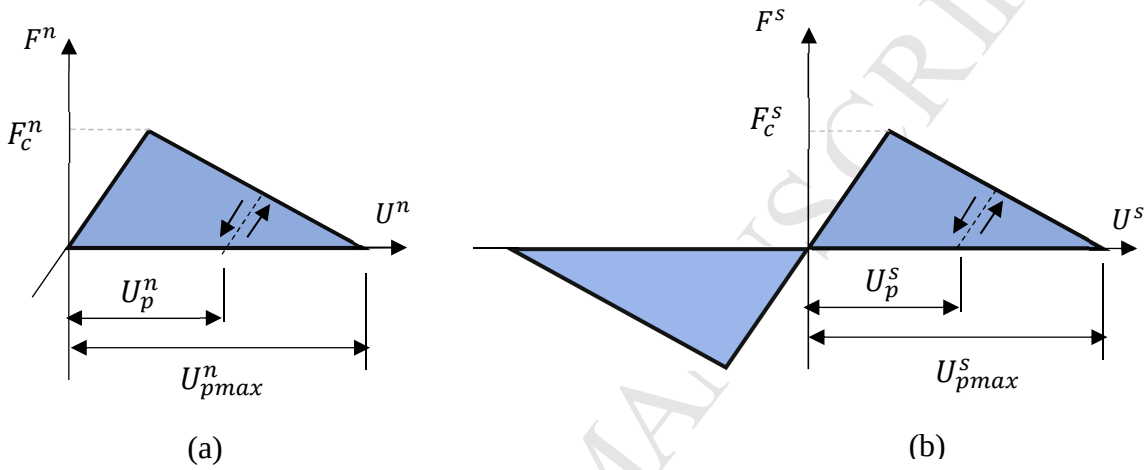

Fig.3 Constitutive behaviour of contact displacement-softening model: (a) normal behaviour, and (b) shear behaviour.

3. Calibration of DEM models

In continuum mechanics based models, the input properties obtained from experimental tests, such as modulus and strength, are directly used. However, in a DEM model with randomly packed particles, there is no rigorous formula to correlate the micro-parameters (contact and particle stiffness as well as bond strength) in DEM with the real material properties. In general, the relation between micro-parameters that characterise a DEM model and macro-properties (such as elastic constant and peak strength) is found by means of virtual calibration tests, such as uniaxial compression test and tension test. Each micro-parameter is related to a relevant material property and it is trialled in order to match the virtual macro-properties gained from the DEM specimen with those of the real material. This process is repeated in different virtual tests until all the necessary macro-properties are matched.

3.1 Generation of DEM specimen

Sample preparation is a step of particular importance in DEM modelling. The two dimensional samples used in this section are square with a dimension of 63 μm × 63 μm. Many packing methods have been proposed in previous studies [26-28]. In the present study, a *radii expansion* procedure is used [25]. This method starts with placing an initial set of particles with artificially small radii in a square area enclosed by four rigid frictionless walls

(see Fig. 4a). The particle size varies from 0.1 μm to 0.166 μm according to a uniform distribution, which is sufficiently small to ensure adequate particles cover the region between fibres, as will be seen later in this paper. The particles are then expanded by increasing their radius by a multiplier factor of two until the desired porosity is achieved. The formula bellow is used to calculate the radii multiplier, m, in order to change the porosity of the space from initial assumed porosity, n_0, to the desired porosity, n.

$$m = \sqrt{\frac{1-n}{1-n_0}} \tag{21}$$

Finally, a number of computation cycles are executed to bring the system into equilibrium. This method has been used by many other researches [29-31] to generate densely packed particle assemblies and readers can refer to [25] for more details. The numerical specimen studied in this section consists of 16,451 particles and the histogram of the particle sizes, as shown in Fig.4, confirms a uniform distribution.

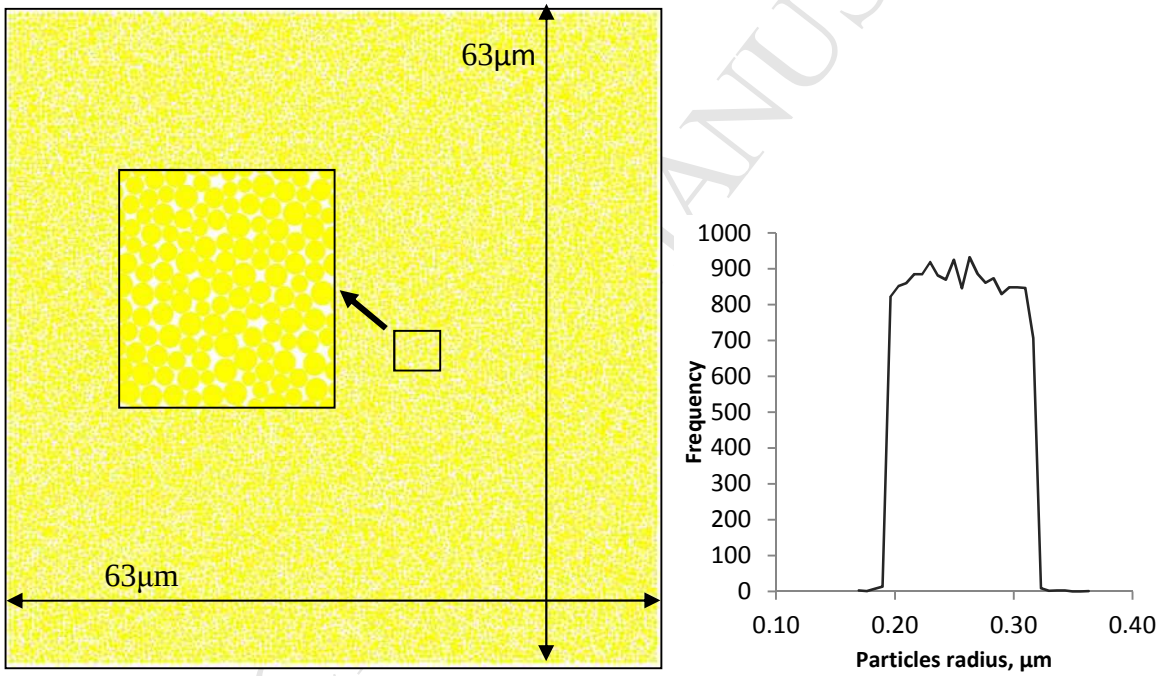

(a) (b)

Fig.4 The DEM model: (a) model geometry and particle assembly, and (b) particle size distribution.

Once the sample is prepared, numerical tests shown in Fig.5 are conducted to find the relationship between the DEM micro-parameters and the material macro-properties. The uniaxial compression test is conducted by moving the right and left rigid walls at a constant and very small velocity (see Fig.5a). Whilst in the direct shear test, the boundary particles are first identified and then assigned with a constant velocity to produce shear displacement, as shown in Fig.5b. The applied loading rate needs to be slow enough in order to maintain the sample in quasi-static equilibrium state during the test and should be stable so as to not

induce any possible dynamic strains [32]. On the other hand, using too small loading rate would be computationally expensive. If not indicated otherwise, the loading rate used throughout this paper is "5 mm/s", which could be considered as a fast one in the real experimental tests. However, since DEM is based on small time integration scheme, time step Δt is chosen in each cycle to be very small (*e.g.*1×10^{-9}s). In other words, with a loading velocity of 5 mm/s and a time step of 1×10^{-9} s, 20,000,000 steps are needed to move the boundary to a distance of 0.1 mm.

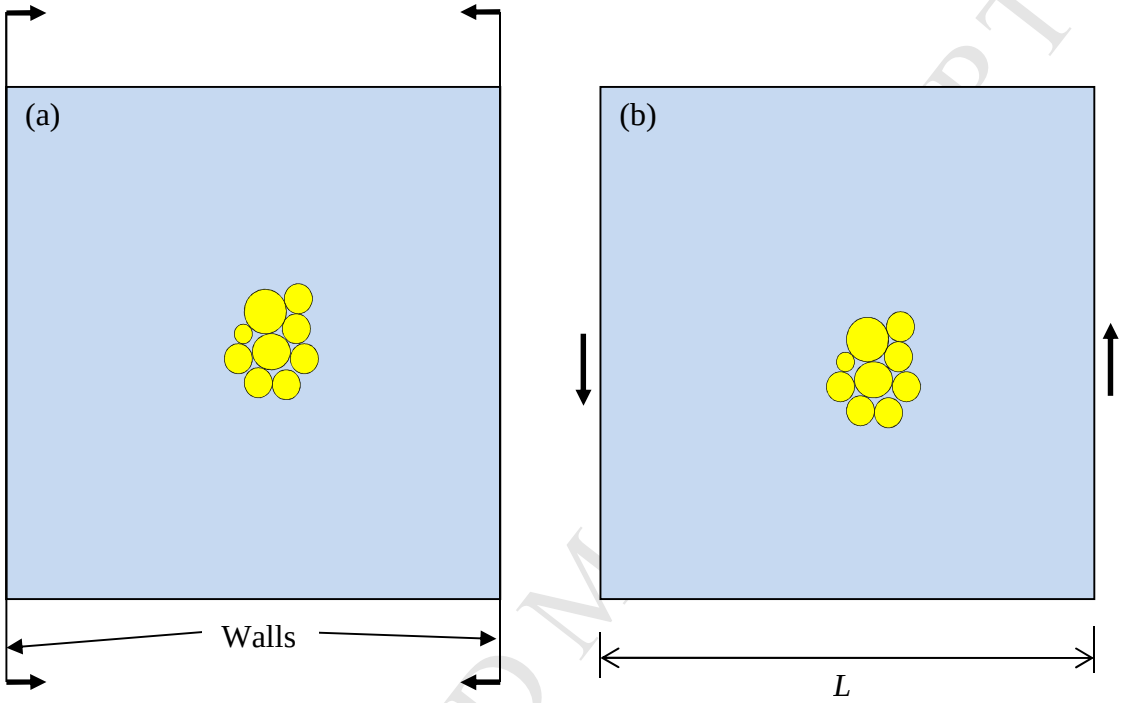

Fig.5 Virtual uniaxial tests of a DEM model: (a) compression and (b) shear.

3.2 Parametric study of contact stiffness

Generally the mechanical properties of an elastic material can be characterised by its elasticity (*i.e.*, elastic modulus, shear modulus and Poisson's ratio) and strength (*i.e.*, compressive strength, tensile strength and shear strength). It has been found that local elastic parameters of particles and contacts, *e.g.*, particle stiffness and parallel bond stiffness, mainly affect the macroscopic elastic response of the entire DEM model, therefore calibrations are required [25]. As the DEM model of a composite lamina consists of two constituents (fibre and matrix) with different properties, each constituent needs to calibrated individually before combing them together with interface stiffness which is assumed equal to that of fibres [13]. Usually the macroscopic Young's modulus of the matrix or fibres is directly proportional to the stiffness of particles (k^n, k^s) and parallel bonds ($\bar{k}^n, \bar{k}^s$). While the macroscopic Poisson's ratio is directly proportional to the ratios of k^n/k^s and $\bar{k}^n/\bar{k}^s$ [25]. The material used in this paper is MY750 epoxy matrix reinforced by E-glass fibres which is chosen from the World Wide Failure Exercise (WWFE) [33]. Both matrix and fibres are considered isotropic and their mechanical properties are given in Table 1.

Table 1 Mechanical properties of fibres and matrix.

Fibre	Transverse modulus, E_f (GPa)	74
	Poisson's ratio, v_f	0.2
Matrix	Modulus, E_m (GPa)	3.35
	Shear Modulus, G_m (GPa)	1.24
	Poisson's ratio, v_m	0.35
	Compressive strength, Y_{mc} (MPa)	120
	Tensile strength, Y_{mt} (MPa)	80

As the aim of this paper is to investigate the transverse behaviour of composite laminae, the 2D DEM modelling is thus carried out under plane strain condition. The elastic properties given in Table 1 are measured under plane stress condition [6] and they can be converted to properties under 2D plane strain condition by [34]:

$$\bar{v}_{f,m} = \frac{v_{f,m}}{1 + v_{f,m}} \tag{22}$$

$$\bar{E}_{f,m} = E_{f,m}(1 - \bar{v}_{f,m}^2) \tag{23}$$

Using Eqs (22) and (23) together with the material properties in Table 1, the Poisson's ratio and Young's modulus for both fibre and matrix under plane strain condition are calculated as $\bar{v}_f = 0.166$, $\bar{E}_f = 71.96$ GPa, $\bar{v}_m = 0.259$ and $\bar{E}_m = 3.12$ GPa, respectively.

In the calibration process, it is convenient to define a ratio between the normal and tangential stiffness for both particles and parallel bonds as:

$$\alpha = \left(k_n^{(A)}/k_s^{(A)}\right)_{particles} = \left(\bar{k}^n/\bar{k}^s\right)_{parallel\ bonds} \tag{24}$$

Fig. shows the relationship between the ratio α and macroscopic elastic properties obtained from axial compressive tests of the DEM model of matrix when normal stiffness for particles and parallel bonds are kept constant at 3.12 GPa. It can be seen that as α increases the Young's modulus decreases while Poisson's ratio increases for the chosen range of values. As both elastic modulus and Poisson's ratio vary with α, the calibration is carried out as follows. First, the value of α is chosen from Fig.6a to produce the desired Poisson's ratio. Then, α is kept constant and a series of simulation tests are conducted with a range of normal stiffness ($K^n = k_n^{(A)} = \bar{k}^n$) as shown in Fig.b. As can be seen in Fig.b the Poisson's ratio is independent of K^n and remains constant for all chosen K^n, whereas Young's modulus increases with the K^n. The target value of $\bar{E}_m$ can then be found.

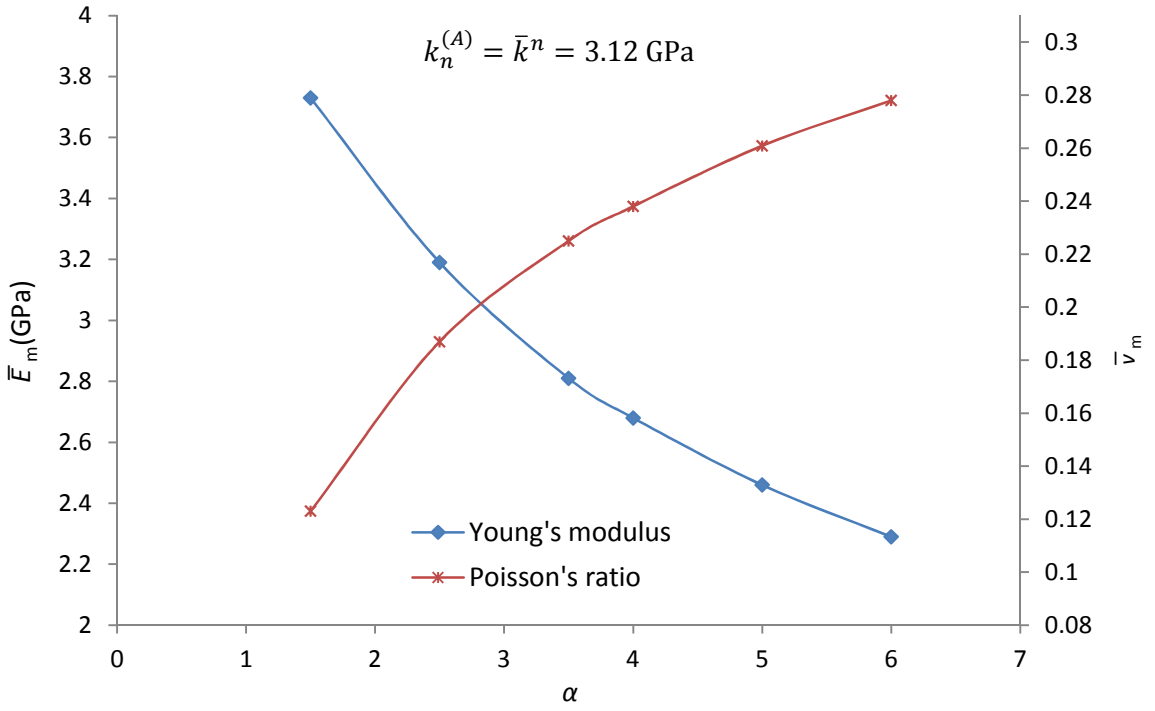
$k_n^{(A)} = \bar{k}^n = 3.12$ GPa
$\bar{E}_m$(GPa)
$\bar{\nu}_m$
α
Young's modulus
Poisson's ratio

(a)

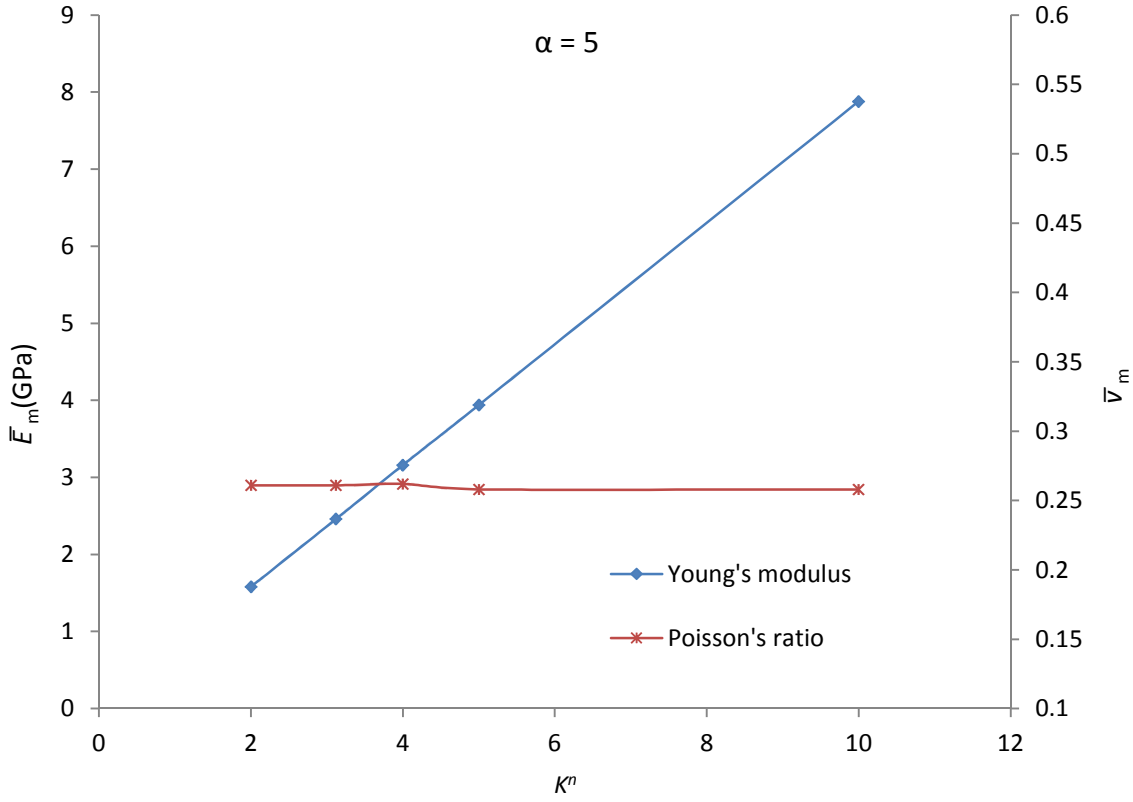
α = 5
$\bar{E}_m$(GPa)
$\bar{\nu}_m$
K^n
Young's modulus
Poisson's ratio

(b)

Fig.6 (a) Influence of normal stiffness to shear stiffness ratio, α, on the Young's modulus and Poisson's ratio; (b) Effect of normal stiffness on Young's modulus and Poisson's ratio.

Same procedure is repeated to find the elastic properties of fibre and the microscopic parameters obtained are provided in Table 2.

Table 2 Micro-parameters for particles and parallel bonds.

		Fibre	Matrix
Particles	$k_n^{(A)}/k_s^{(A)}$	2.5	5
	$k_n^{(A)}$ (GPa)	70	4
Parallel bond	$\bar{k}^n/\bar{k}^s$	2.5	5
	$\bar{k}^n$ (GPa)	70	4

In order to further verify these parameters, a numerical shear test is performed on the DEM model to predict the shear modulus, $\bar{G}_m$, of the matrix. The elastic properties for both fibre and matrix obtained from DEM are very close to those from experimental [33] as listed Table 3.

Table 3 DEM predictions of the elastic properties of fibre and matrix.

	Experimental [33]	DEM	Error (%)
$\bar{E}_f$ (GPa)	71.96	72.2	0.33
$\bar{\nu}_f$	0.166	0.170	2.3
$\bar{E}_m$ (GPa)	3.12	3.16	1.2
$\bar{\nu}_m$	0.259	0.262	1.1
$\bar{G}_m$ (GPa)	1.24	1.21	2.4

3.3 Parametric study of bond strength

In order to enable the DEM model to predict the failure behaviour of a material, it is also necessary to correlate the local bond strength parameters to the DEM model's macro strength. Normally two failure modes are predominating in composite laminae under transverse loading, *i.e.*, matrix cracks and fibre/matrix debonding. The matrix compressive strength, Y_{mc}, is given in Table 1. Mohr-Coulomb failure criterion has been widely used to describe the plastic deformation of the epoxy matrix [7, 20, 21], and is adopted to determine the strength of the parallel bonds for the matrix in the DEM model. When using the contact softening model to represent the fibre/matrix interface, both interfacial strength and fracture energy must be known. Unfortunately, these properties are difficult to obtain from simple laboratory experiments [35]. In this study, the interfacial strength is assumed to be equal to the cohesion of the matrix, c, and according to the Mohr-Coulomb failure criterion the relationship between the cohesion and matrix strength is given by:

$$c = Y_{mc}\frac{1-\sin\varphi}{2\cos\varphi} \tag{25}$$

where φ is the friction angle and can be related to the fracture surface angle ξ by:

$$\xi = 45 + \varphi/2 \tag{26}$$

Typically $50^0 < \xi < 60^0$ is found for epoxy matrices [7], and thus φ is between 10° and 30°. Assuming $\varphi = 23^0$ gives a cohesion c of 39.7 MPa. Wang and Tonon [36] found that micro tensile strength of the bond directly determines the strength of material regardless the magnitude of bond shear strength. Therefore, for simplicity $\bar{\sigma}_c = \bar{\tau}_c$ is assumed. Then a series of uniaxial compression tests are carried out with different bond strength values to find the relationship between bond strength and material strength, as shown in Fig.7. The macro strength of the DEM model is the maximum value of axial stress acting on the walls at peak load. Fig.7 indicates that macro strength increases linearly with the bond strength. At this stage, the smallest time step Δt_1 is used. The effect of time step on macro compressive strength is studied in the next section.

3.4 Parametric study of time step

An important consideration in the DEM modelling is the time step. DEM uses a central difference time integration approach to solve the equations of particle motion, and to maintain a stable integration the time step must not exceed the critical time step Δt_{crit}:

$$\Delta t_{crit} < \sqrt{m/K} \tag{27}$$

where K is the contact stiffness and m is the particle mass. Choosing a suitable time step is of particular importance because it has direct effect on the total computational time. The effect of time step on the macro strength is therefore investigated, trying to find a large but still valid time step and thus reduce the computational time. Three values of time step are chosen, $\Delta t_1 = 9.3 \times 10^{-11}$s, $\Delta t_2 = 1 \times 10^{-10}$ s and $\Delta t_3 = 1 \times 10^{-09}$s. The first one is the default value calculated by the software itself [25] based on mass of particles and contact stiffness according to Eq. (27). Note that, for all time steps, the loading velocity is kept constant at 5 mm/s. Fig.7 shows the macro strength of the sample under these three different time steps, with matrix compressive strength and cohesion also plotted. It is demonstrated that the strength values are almost identical for all time steps for low bond strength. The two cases with Δt_2 and Δt_3 almost give the same strength while they are both diverted from Δt_1 about 10% at bond strength of 85 MPa. Thus the choice of time step needs to be further investigated by plotting out the complete stress-strain curves in the later section of modelling failure process.

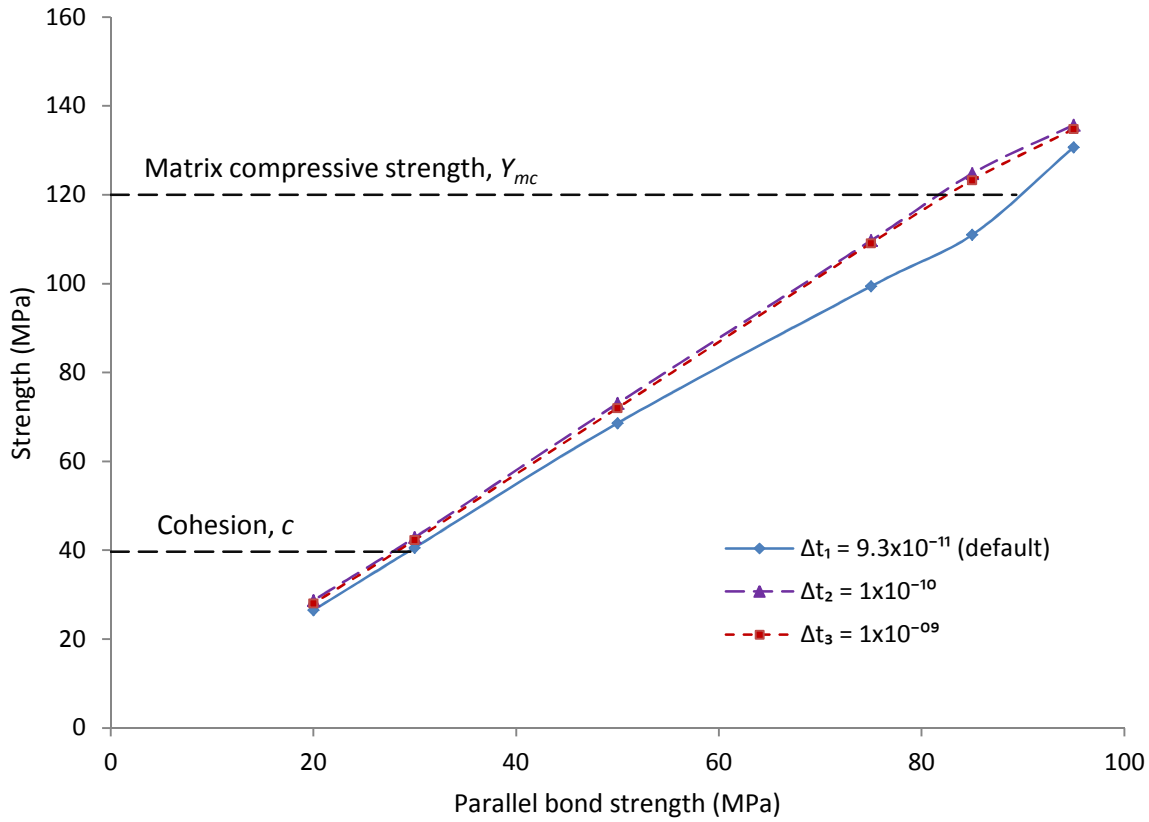

Fig.7 Influence of bond strength and time step on the macro compressive strength of a DEM model.

4. DEM modelling of damage evolution in RVEs under transverse compression or transverse shear load

4.1 Prediction of effective elasticity

Before performing any simulations to predict the failure of composite materials, it is important to ensure that DEM is capable of accurately predicting the effective elastic properties. To investigate the size dependence of the elastic properties, a set of representative volume element (RVE) with different size are generated using the approach developed in previous study [37] which can overcome jamming limit and can be used for fibres with any inter distances. In each RVE, variable fibre diameters are used according to a normal distribution with a mean fibre diameter of 6.6 μm and a standard deviation of 0.3106. A typical RVE of DEM model under transverse compression and transverse shear is illustrated in Fig.8. Regarding the size of RVE, González and LLorca [7] suggested that an RVE size of 63 μm × 63 μm is large enough to accurately represent the macroscopic material. This suggested size is adopted first and the effective elastic properties are then computed for different RVE sizes range from 30 μm × 30 μm to 100 μm × 100 μm, trying to identify the smallest valid RVE in order to reduce DEM computational time. Each RVE consists of three phases, *i.e.*, matrix, fibre and interface. Calibrated micro DEM parameters for matrix and fibres in Table 2 are used, and the micro DEM parameters for the fibre/matrix interface are assumed to be the same as those of fibres.

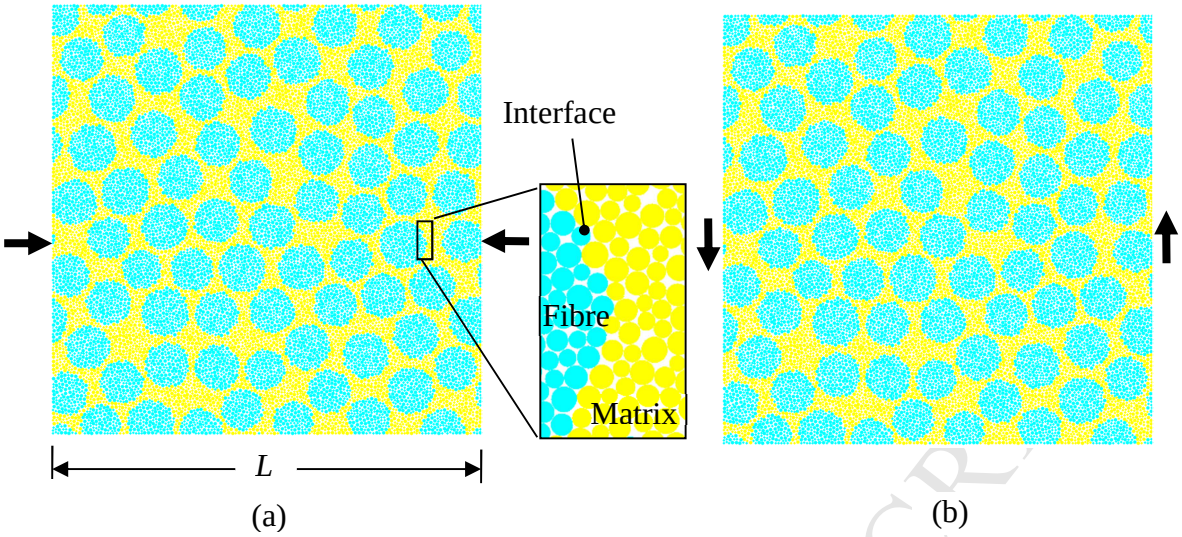

Fig.8 A RVE of DEM model subjected to: (a) transverse compression and (b) transverse shear (arrows indicate the loading directions).

Fig.9 shows the elastic properties calculated using different RVE sizes. The RVE of each size is tested five times, and each time the RVE has a different random distribution of fibres. The secondary horizontal axis δ on the top represents the relationship between the side length of RVE, L, and the mean fibre radius, r_f, as:

$$\delta = \frac{L}{r_f} \tag{28}$$

As can be seen from the Fig.9, both Young's modulus and shear modulus of the RVE with a size of 63μm × 63 μm are close to the experimental results with little differences from one model to another. The discrepancy is likely caused by the change of fibre arrangements, which leads to increase or decrease of the number of contacts and particles representing the fibres, matrix and interface. However, our DEM model still gives good predictions of Young's modulus and shear modulus, compared with FEM using the same approach for generating random fibre distributions [37]. In this study, the predicted Poisson's ratio seems more sensitive to RVE size and the variation could reach 19%. Similar findings from other numerical models have also been reported. For instance, Wongsto and Li [38] found that the predicted effective properties using various theoretical and numerical methods were smaller than the experimental data.

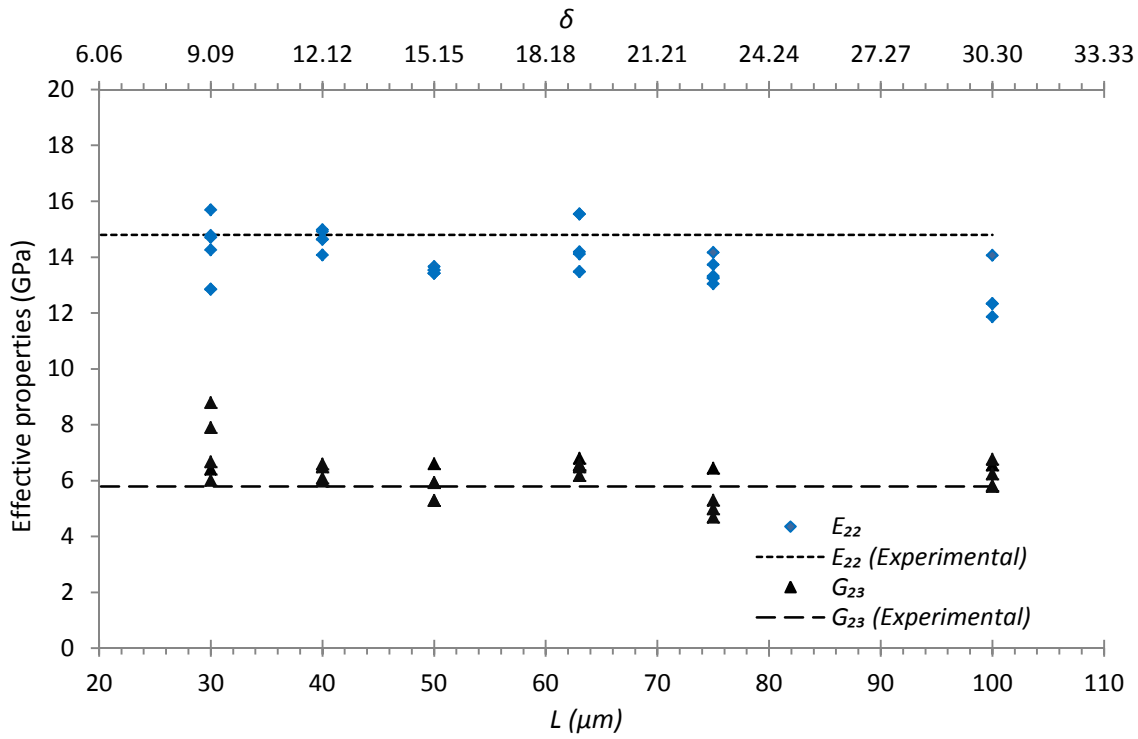

(a)

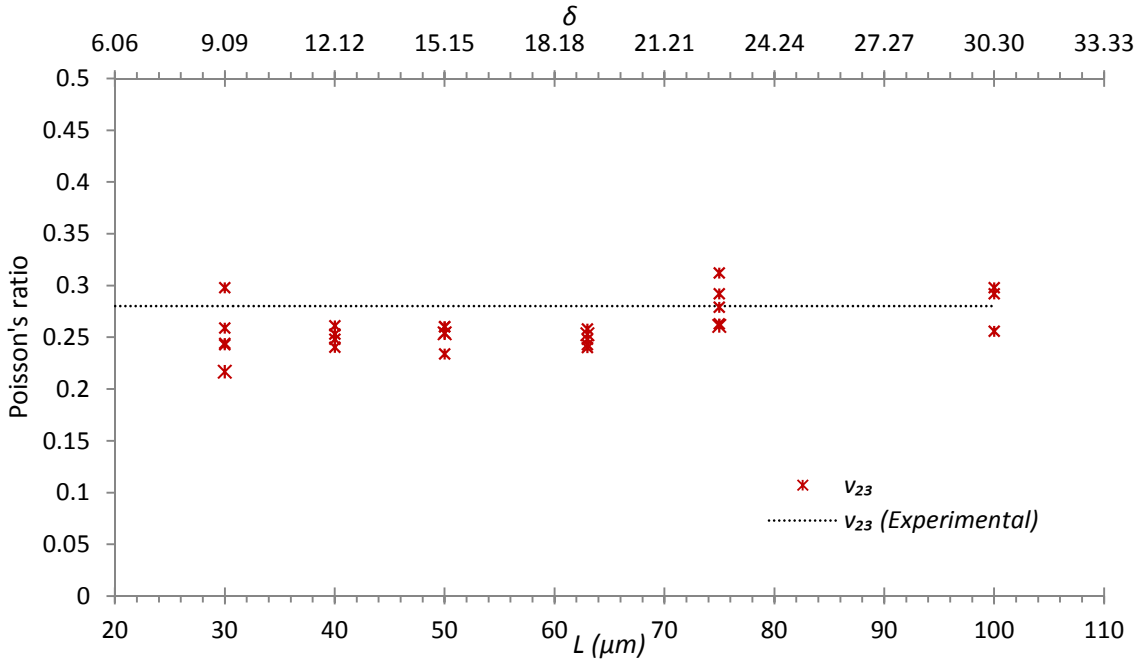

(b)

Fig.9 DEM predictions of elastic properties using different RVE sizes compared to experimental results [33]: (a) Young's modulus and shear modulus, and (b) Poisson's ratio.

4.2 Prediction of stress-strain curves and damage progression under transverse compression

In this section the failure of RVEs subjected to transverse compression is studied. The RVEs used in this section and next section have an identical size of 63 μm × 63 μm. The effect of time step on the stress-strain curve of a typical RVE, which is of particular importance for saving computational time, is examined in Fig.10. Within the elastic region (under 20 MPa), the simulation results are almost identical and agree well with the experimental one. The final failure appears to become more brittle when time steps are reduced, confirming that small time steps lead to better redistribution of the stress within the system and the model is more stable. For all the DEM simulations in Fig.10, the mean compressive strength is 156.3 MPa which is greater than experimental result by 7%. Therefore, the time step of $\Delta t = 1 \times 10^{-9} s$ will be used in later simulations. The nonlinear mechanical response of the stress-strain of the DEM model is not well captured comparing with experimental data. The nonlinear behaviour of the curve would be more obvious in case of longitudinal shear and off-axis loading. However, the nonlinear contact law could be introduced in the future to solve the problem. While geometric nonlinearity (e.g. fibre rotation) is not important under transverse loading.

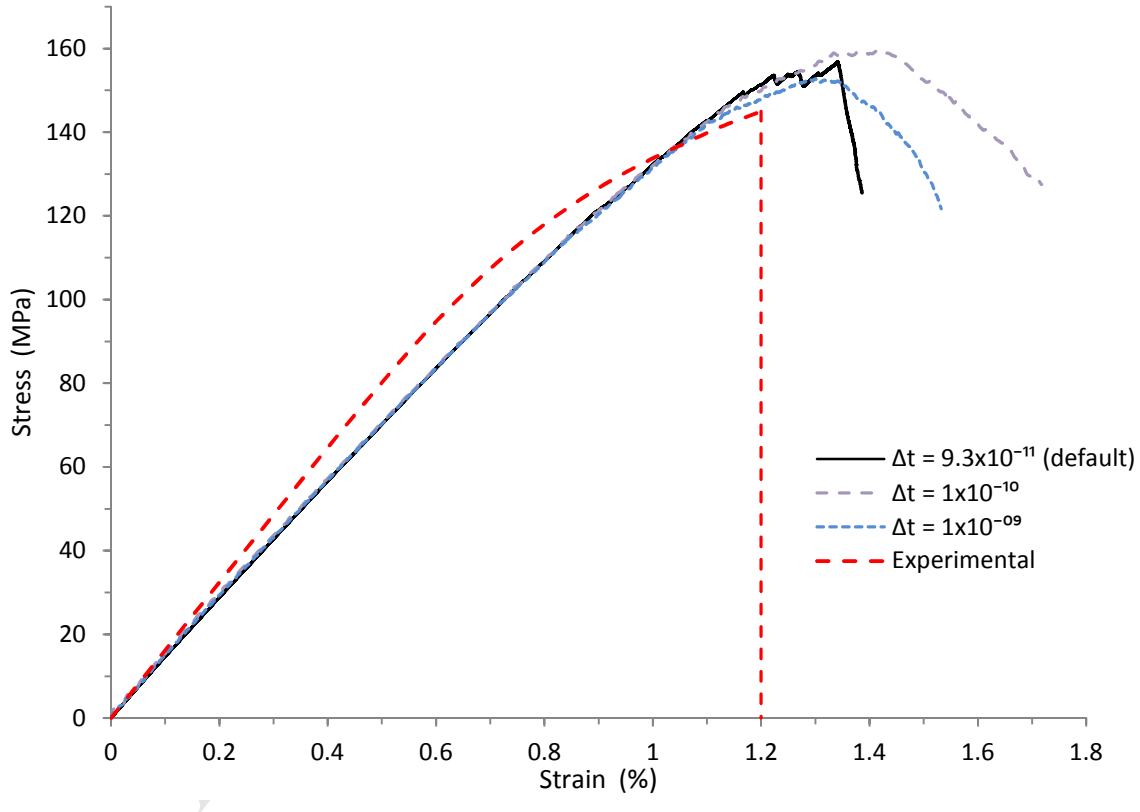

Fig.10 Stress-strain curves from DEM simulations using different time steps compared to experimental results [33].

The influence of fibres distribution in the RVEs on the mechanical response is also studied by comparing the results obtained from five different fibre arrangements. The stress-strain curves of all five RVEs under transverse compression are shown in Fig.11. It can be seen that

the failure strength ranges from 151 MPa to 167 MPa giving the smallest and the largest differences of 4% and 14%, respectively, in comparison with the experimental results. An interesting outcome of using DEM is that the transverse compressive failure strains of the RVEs are also obtained whilst they have not been reasonably achieved in previous studies using FEM due to numerical convergence difficulties [7, 22, 39]. To show the accuracy of the DEM modelling, the results are also compared with two recent FEM models [7, 40] in Fig.11.

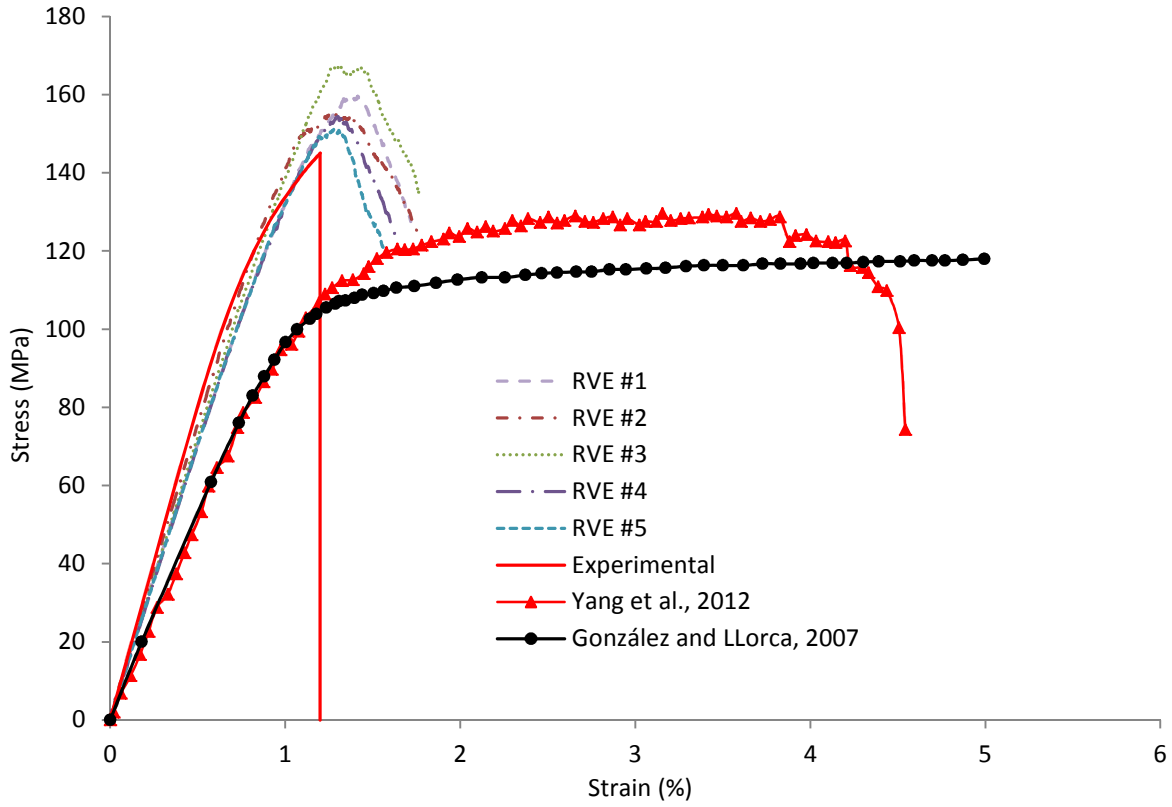

Fig.11 Stress–strain curves of five RVEs under uniaxial compression.

Another major feature of DEM modelling is its capability to predict and visualise the damage initiation and propagation process. Taking RVE #3 as an example, Fig.12 shows the damage progression in the composite under transverse compression, where a stress-strain curve and the damage profiles corresponding to the three characteristic loading points are also included. Point (a) in the stress-strain curve represents the state of a loading strain of 0.7% and its corresponding damage pattern is shown in Fig.12a. It can be seen that the fibre/matrix debonding (indicated by red dots) appears to be the major damage mechanism at this stage. After this point, the matrix cracks starts to appear, especially in the highly stressed areas where fibres are too close. The cracking leads to certain fluctuations in the stress-strain curve as indicated from the figure. Then, interfacial debonding and matrix cracks are emerged throughout the RVE before reaching the peak strength, as shown in Fig.12b. The inclination angle α_c of the critical plane is about 53° at this point, and it is a little smaller than the failure plane angle ξ=56.5° calculated from Eq.(26). Finally, more matrix cracks appear with further increase of loading and the final failure is shown in Fig.12c. From the last graph one can see that there are several possibilities for developing a critical plane across the RVE. The failure mode shown in Fig.12c is similar to the final accumulated failure of the RVE in FEM when

perfectly plastic matrix assumption is used [19]. However, it is quite different from those models using other failure criteria to represent matrix yielding, such as Mohr-Coulomb model [7] and Drucker-Prager [40].

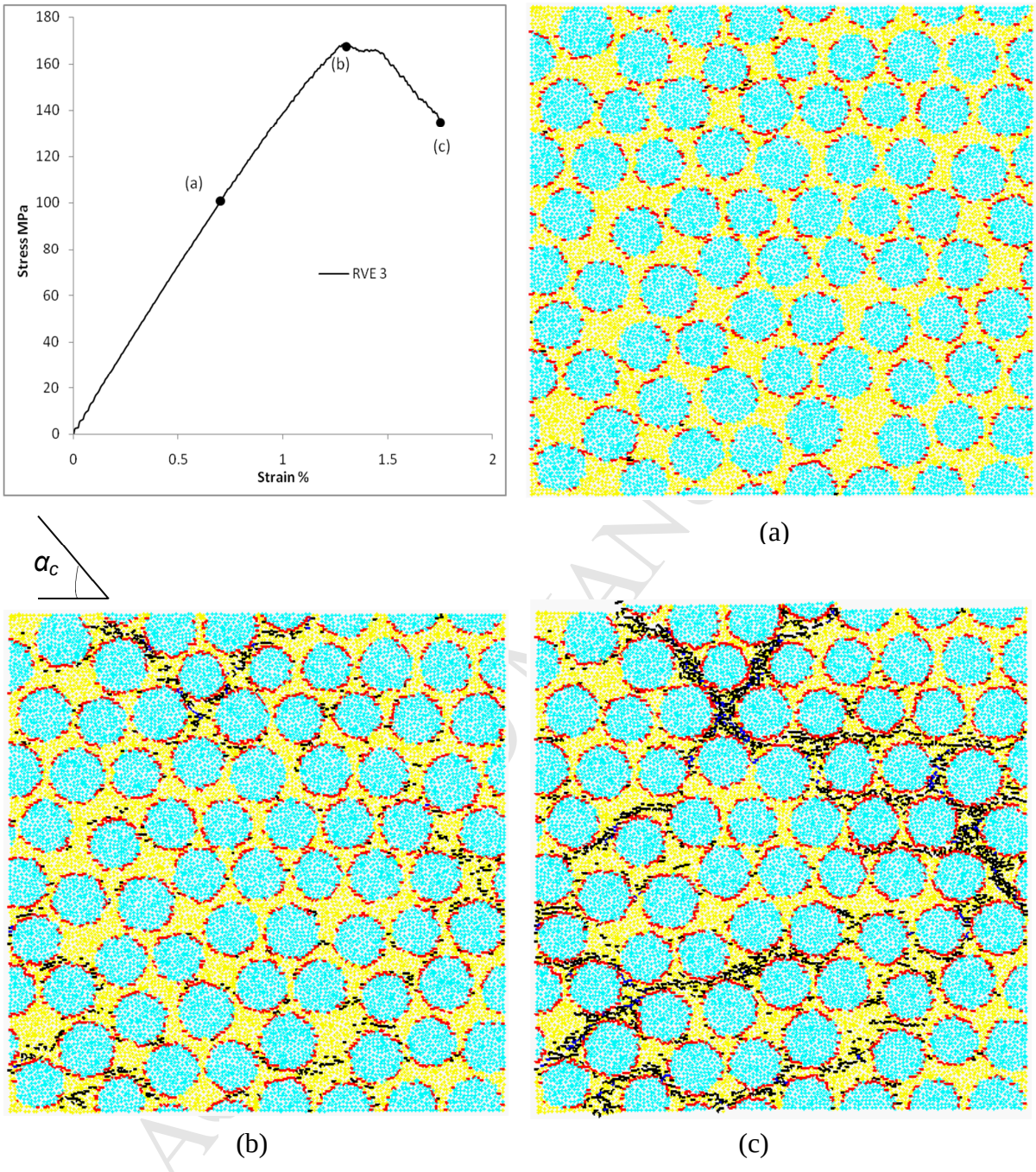

Fig.12 Damage evolution under transverse compression at different loading strains: (a) 0.7% (b) 1.3% (c) 1.7%. (Red dots are fibre/matrix debonding and black dots are matrix cracks)

4.3 Prediction of stress-strain curves and damage progression under transverse shear

It is very difficult to carry out a laboratory test on a composite lamina/laminate under transverse shear. Finding a robust numerical method to simulate the test is then always

beneficial, in particular, to capture the behaviour of the lamina until failure. Many factors could alter the damage behaviour of a lamina under transverse shear including fibre arrangements and fibre/matrix interface properties. Attempts have been made by researchers to find a relationship between the transverse shear strength and transverse compressive strength. Some researchers assumed the transverse shear strength, S_T, to be half of the compressive strength, Y_C, *i.e.*, $S_T = 0.5\,Y_C$ [6], where Y_C is the transverse compressive strength of the lamina. This is also adopted in this study. The transverse compressive strength of the lamina is 145 MPa (see experimental stress-strain curve in Fig.10), therefore, we assume that $S_T = 72.5$ MPa.

The transverse shear of five different RVEs with different fibre distribution is modelled and the stress-strain curves are shown in Fig.13, along with the FEM results extracted from [19] and [41] for comparisons. The figure shows that all the stress-strain curves from DEM modelling are almost identical and linear before reaching a loading stress of 35 MPa. A short line depicts the experimental initial shear modulus is also plotted. It is evident that the current simulation results are closer to the experimental shear modulus. After this point, the stress-strain curves of the RVEs start to divert from each other. This discrepancy is attributed to the development of micro-cracks that, similar to what was observed from the simulations of transverse compression described in the previous section, depends on the fibre distributions. The shear failure strength slightly varies for different fibre arrangements. In addition, for all the RVEs in Fig.13 the mean shear strength is 70 MPa, which is just slightly smaller than experimental result of $S_T = 72.5$ MPa, and about 9% less than the strength predicted in [19] and about 19% higher than that from [41] .

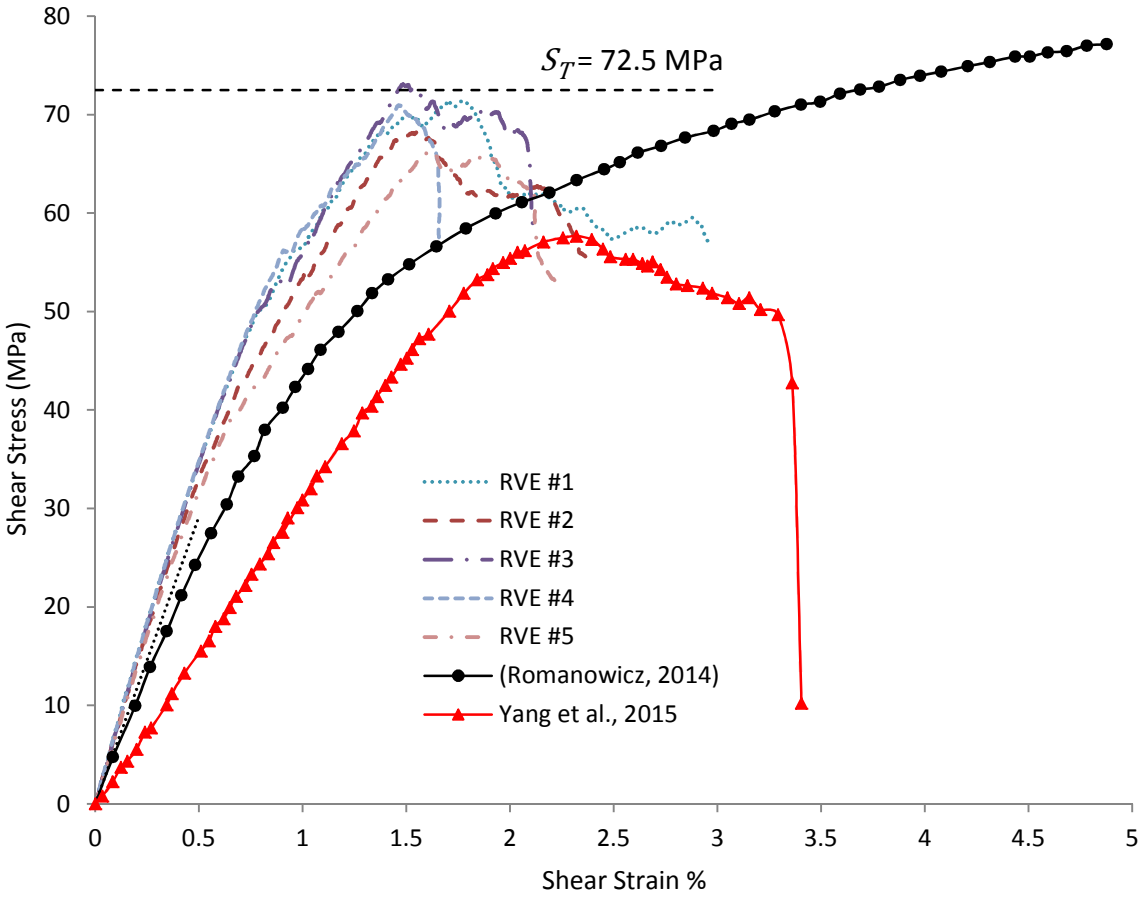

Fig.13 Transverse shear stress-strain curve using five different fibre arrangements compared with [19] and [41].

While the stress-strain curve and damage evolution in RVE #3 under transverse shear is shown in Fig.14. The stress-strain curve drops at point (a) due to matrix cracking at the right-bottom of the RVE close to the edge. However, this crack does not propagate longer because it is constrained by the two surrounding fibres. After this point, more interfacial debonding occurs until the peak point (b). Afterwards, matrix cracks appear mainly in the middle of the RVE and propagate fast and diagonally between fibres, leading to the ultimate failure at point (c).

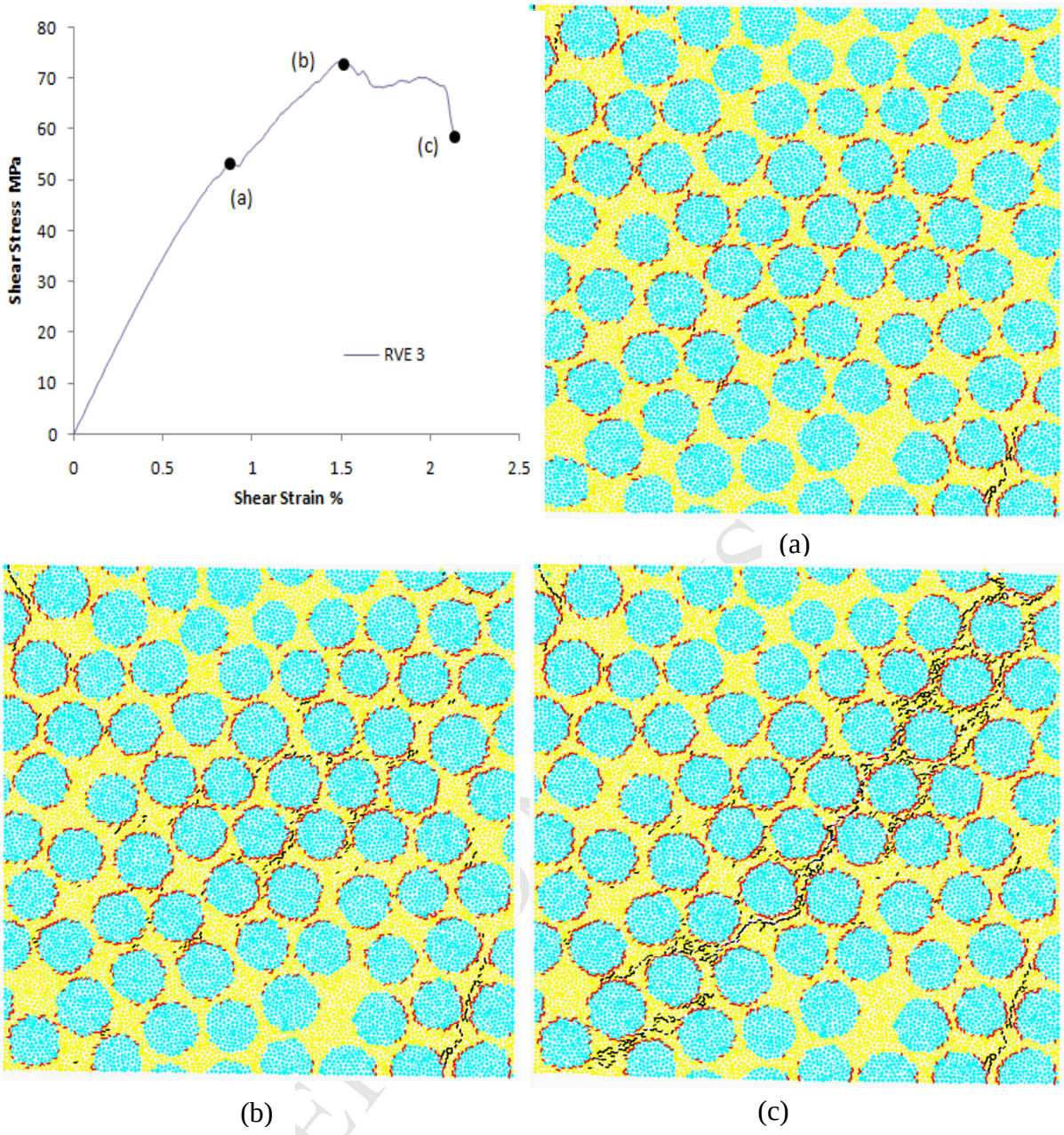

Fig.14 Damage evolution under transverse shear of RVE #3 at different strain stages: (a) 0.87%, (b) 1.51%, and (c) 2.13%. (Red dots are fibre/matrix debonding and black dots are matrix cracks)

4.4 Effect of RVE size on failure strength and failure strain

As an attempt to reduce the computational cost, RVEs with sizes smaller than 63 μm × 63 μm are simulated. Variations of compressive strength for five different RVE sizes are shown in Fig.15a. The results show that the size of RVE has slight influences on the failure strength and there is no obvious trend of convergence for the RVE size. The smallest RVE of 30 μm × 30 μm is most diverted away from the experimental result, while the RVE of 50 μm × 50 μm, has a mean compressive strength closer to the experimental result than 63 μm × 63 μm.

Fig.15b shows the failure strains for the RVEs of different sizes. The overall trend of results tends to be higher than the experimental one and the smallest RVE has the largest difference.

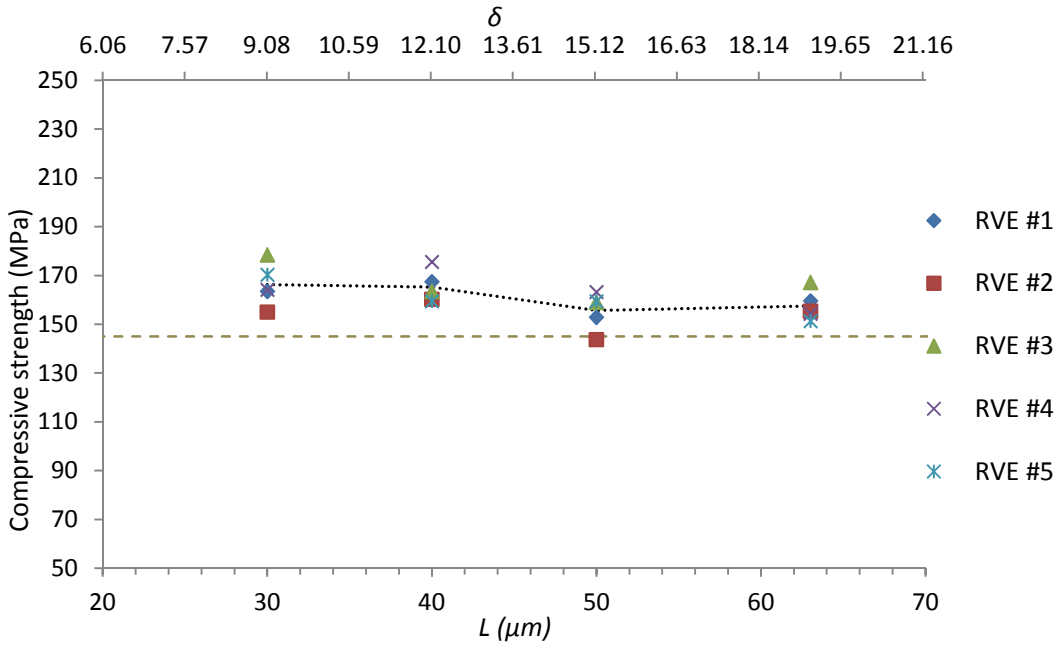

(a)

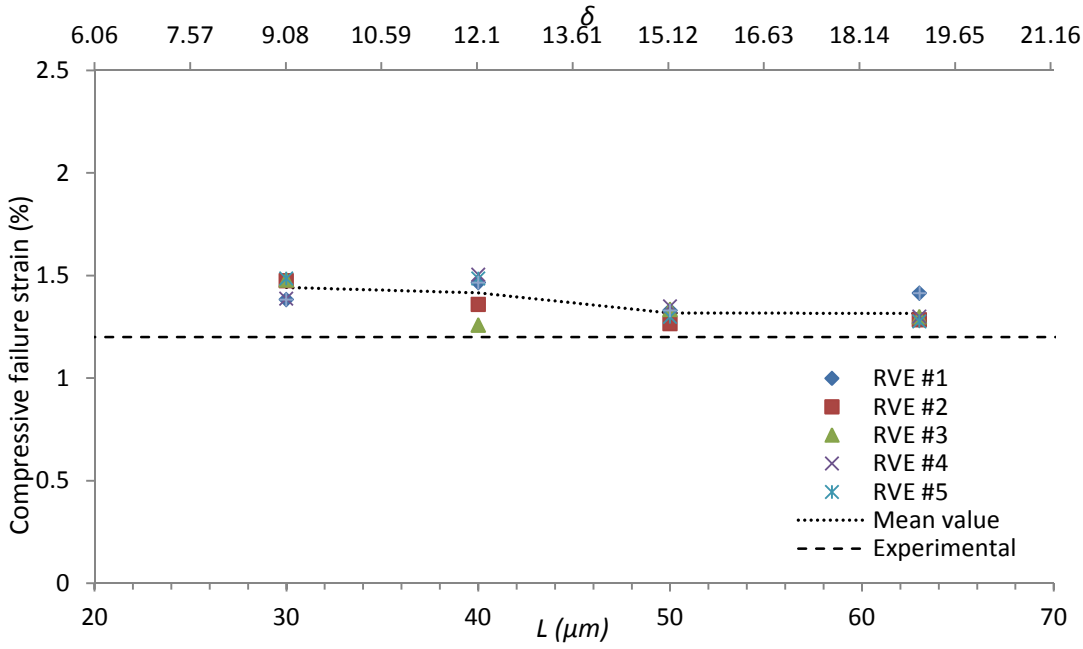

(b)

Fig.15 Variation of compressive strengths and transverse compressive failure strains with RVE size, compared with experimental data [33]: (a) compressive strengths, and (b) transverse compressive failure strains.

Fig. 16 shows the variation of transverse shear strength with RVE sizes. As can be seen from the figure, the mean values of shear strength of the five RVEs show fluctuations rather than clear convergence towards $S_T = 0.5\ Y_C$, although the closest mean shear strength is from the largest RVE of 63 μm × 63 μm. In summary, the RVEs of 63 μm × 63 μm give overall better predictions of failure strength and failure strains, and this further confirms an RVE size of 63 μm × 63 μm should be used in the next sections of DEM simulations of biaxial loading.

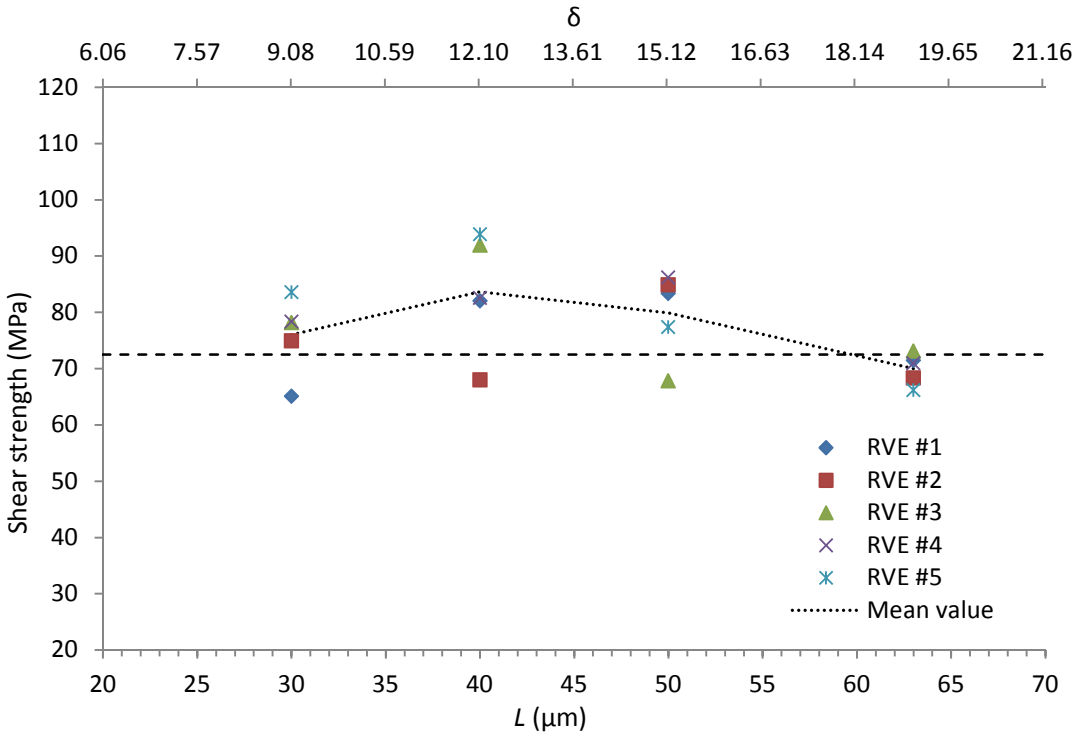

Fig.16 Transverse shear strength of RVEs with different sizes.

5. DEM modelling of RVEs under biaxial loads

The ultimate goal of this paper is to visualise the damage evolution and predict the failure envelop of composite laminae under biaxial loads. An accurate and reliable failure criteria have been pursued for the past few decades, and an effort has been made by the organisers of the first [2, 42] and second [1] WWFE to compare the experimental results with the predictions from different failure criteria. 19 failure criteria were evaluated and ranked according to their capability to predict the stress-strain curves under different uniaxial loading as well as the failure envelope in a series of test cases including biaxial loading. The comparisons revealed that the predictions of many failure criteria varied considerably from experimental results. WWFE also highlighted the importance of capturing the progressive failure in composite laminates. Generally, it was found that most failure criterions performed well when damage initiates in a single ply followed intimately by the catastrophic failure, or brittle failure. However, most criterions were not accurate enough when noticeable nonlinearity occurred before the final catastrophic failure. Therefore, it is important to develop a suitable numerical method to capture and visualise the entire process of damage initiation and progression in composite laminates.

5.1 DEM prediction of the failure envelope

For the purpose of modelling biaxial loads using DEM, the RVEs are subjected to a combination of transverse normal stress, σ_{22}, and transverse shear, τ_{23}, to obtain σ_{22}-τ_{23} failure envelope. The RVEs have a size of 63 μm × 63 μm. The DEM results are compared with predictions from two theoretical criteria developed by Hashin [3] and Puck and Schürmann [5].

Hashin criterion is one of the early failure theories that can distinguish the fibre and matrix fracture initiation in composite materials, and each is further subdivided into two damage mechanisms, *i.e.*, tensile and compressive failure modes. Assuming isotropic composite lamina in the *y*-*z* (or 23) plane, the two dimensional Hashin failure theory of a lamina under combined transverse normal stress and transverse shear are expressed as:

$$\left(\frac{\sigma_{22}}{Y_T}\right)^2 + \left(\frac{\tau_{23}}{S_T}\right)^2 = 1 \qquad \sigma_{22} \geq 0 \qquad (29)$$

$$\left(\frac{\sigma_{22}}{2S_T}\right)^2 + \left[\left(\frac{Y_C}{2S_T}\right)^2 - 1\right]\frac{\sigma_{22}}{Y_C} + \left(\frac{\tau_{23}}{S_T}\right)^2 = 1 \qquad \sigma_{22} < 0 \qquad (30)$$

where Y_C and Y_T are the transverse compressive and tensile strengths of the composite, respectively, and S_T and S_L stand, respectively, for the transverse and longitudinal shear strength. Despite the capability of this failure criterion for predicting the damage in the lamina under normal and transverse shear, numerous studies over the last decades show that it does not always agree with experimental results accurately, especially the failure envelope studied under combined transverse compression and in-plane shear. This drawback of the Hashin criterion is due to neglecting of determination the actual fracture plane and its orientation. And using a quadratic approach to account for the interaction between the stress invariants may underestimate the material strength, whereas any higher polynomial degree would lead to more complicated expressions. With increasing computational capacity, many models, therefore, have been proposed to improve Hashin criterion including the one proposed by Puck and Schürmann [5]. Puck's model is based on Mohr-Coulomb hypothesis and assumes that fracture is triggered due to the normal stress σ_n and tangential stress τ_t, acting on the failure plane with a specific inclination angle to the material plane, which is the key element of the model. The criterion is expressed as:

$$\sqrt{\left[\left(\frac{1}{Y_T} - \frac{2p_{\perp\perp}(1+p_{\perp\perp})}{Y_C}\right)\sigma_n(\xi)\right]^2 + \left[\frac{2(1+p_{\perp\perp})}{Y_C}\tau_t(\xi)\right]^2} + \frac{2p_{\perp\perp}(1+p_{\perp\perp})}{Y_C}\sigma_n(\xi) = 1 \qquad \sigma_n \geq 0 \qquad (31)$$

$$\sqrt{\left[\left(\frac{2(1+p_{\perp\perp})}{Y_C}\right)\tau_n(\xi)\right]^2 + \left[\frac{2p_{\perp\perp}(1+p_{\perp\perp})}{Y_C}\sigma_n(\xi)\right]^2} + \frac{2p_{\perp\perp}(1+p_{\perp\perp})}{Y_C}\sigma_n(\xi) = 1 \qquad \sigma_n < 0 \qquad (32)$$

with

$$\sigma_n(\xi) = \sigma_{22}\frac{1+\cos(2\xi)}{2} + \tau_{23}\sin(2\xi) \tag{33}$$

$$\tau_t(\xi) = -\tau_{23}\frac{\sin(2\xi)}{2} + \tau_{23}\cos(2\xi) \tag{34}$$

where S_T is the fracture resistance of the fracture plane subjected to the pure transverse shear, ξ is the fracture angle plane, and φ is friction angle as in Eq.(26). The fracture angle plane in the case of biaxial loading is slightly different from that for uniaxial compression in Eq.(26) and given by:

$$\xi = 45 + \frac{\varphi \mp \beta}{2} \tag{35}$$

in which $\beta = \arctan(2\tau_{23}/\sigma_{22})$. Note that in case of uniaxial loading, τ_{23}=0, Eq.(35) is reduced to Eq.(26). $p_{\perp\perp}$ is the inclination coefficient which does not have a clear physical meaning and it is usually fitted to the (σ_n, τ_t) failure slope angle that is experimentally deduced. However, Puck and Schürmann [5] recommended to use $p_{\perp\perp}$ in the range of 0.2-0.25 for a typical glass-fibre/epoxy composites. $p_{\perp\perp} = 0.22$, a value in the middle of the range, is used in the study.

To use these two failure criteria, the material failure strengths are required. In this study, the input failure strengths are those obtained from DEM simulations of RVE #1, given in Table 4.

Table 4 Failure strength used in Hashin and Puck failure criteria.

Y_c (MPa)	159.5
Y_T (MPa)	35
S_T (MPa)	71.5

For biaxial loading, there are certain possible loading paths. For example, the normal and shear loads may be applied proportionally at the same time, or the loading could start by applying uniaxial compression until a required compressive stress, then transverse shear is applied while the compressive stress is kept constant, or vice versa. The effect of loading path on the failure envelope has been investigated experimentally in [43] and numerically using FEM in [44, 45], and all concluded that the loading path did not affect or change the failure envelope significantly. However, the influence of loading path in DEM modelling is not studied in this paper.

Two loading paths are used in this study to simulate a biaxial test in DEM, as shown in Fig.17. The first path (Fig.17a and b) is used to apply transverse tension and shear on the RVE, the results of which are shown in Part-A of Fig.18. Following the same procedure as described in Section 4.3 for the pure shear test, the particles on the right- and left-hand side edges of the RVE are taken as boundary particles that are subsequently subjected to a constant velocity tangent to the edges until the desired shear stress is reached. Once the target

shear stress is reached, the unbalanced force of each particle on the boundary is replaced by an external force of equal magnitude but in the opposite direction, see Fig.17b. Finally, a velocity normal to the edge is taken by the right- and left-hand side boundary particles to apply transverse normal load until the final failure, as shown in Fig.17b. By varying the initial shear stress applied on the boundary particles, the failure envelope of Part-A in Fig.18 is constructed. The second loading process is used to simulate transverse compression and shear quadrant only, *i.e.*, Part-B in Fig.18. In this loading method, the right- and left-hand side walls act as loading platens and their horizontal moving velocity is controlled by a servo-mechanism to maintain a constant transverse compression stress, see Fig.17c. Then, a constant velocity is applied on the right and left boundary particles until the final shear failure, as shown in Fig.17d.

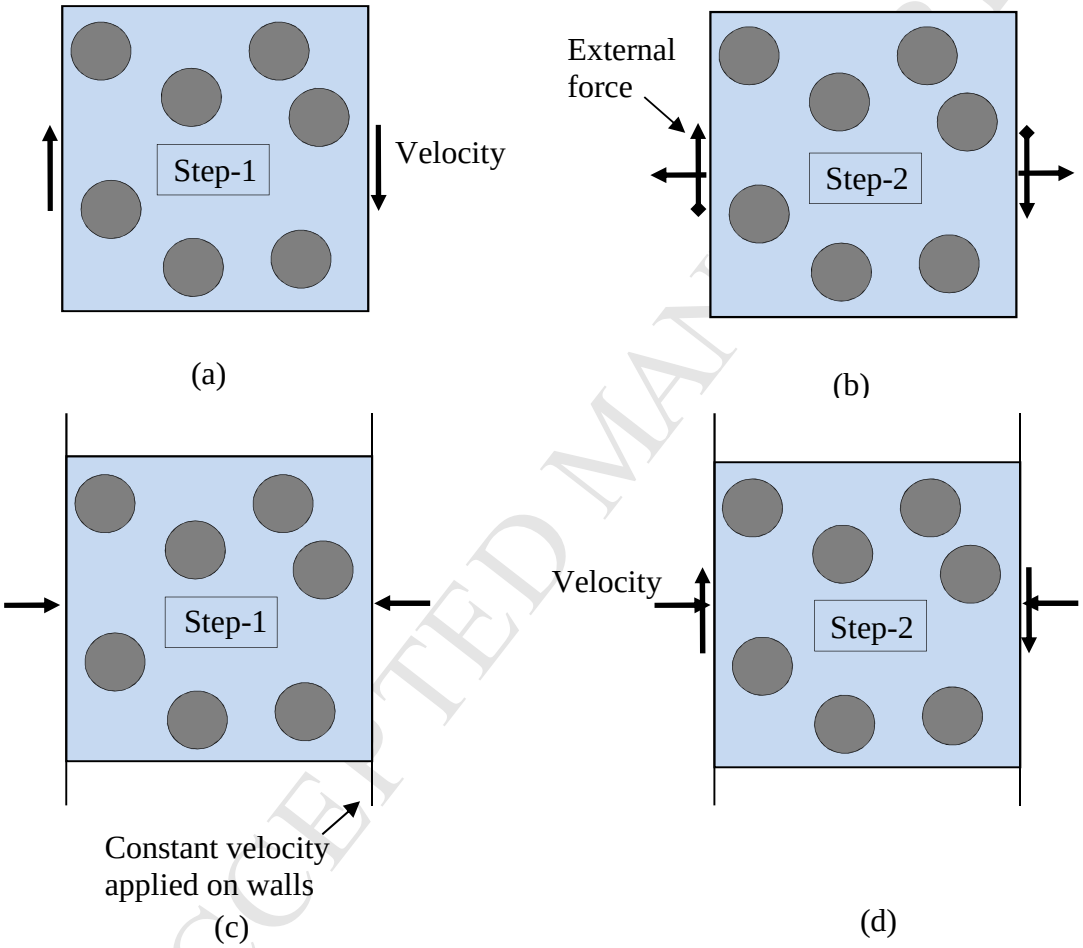

Fig.17 Loading schemes used to perform biaxial tests (arrows ◆→ represent external force and arrows → represent velocity applied): (a)-(b) shear and tension in Part-A, and (c)-(d) shear and compression in Part-B.

In the DEM simulations, the strength is the peak value on the stress-strain curve and the final failure takes place when the curve drops by 20% of the peak point, (*e.g.*, point c in Fig 12a). The corresponding failure envelope is then generated and plotted in Fig. 18 together with the predictions from Hashin [3] and Puck and Schürmann [5] failure criteria.

It can be seen that the strength of the material predicted by DEM is generally lower than that predicted by the two failure criteria when the material is subjected to transverse tension and shear (in Part-A region), while it is higher when the material is subjected to transverse compression and shear (in Part-B region). This is expected since the current DEM modelling has considered residual strength attributed to any friction and contact between the fractured surfaces that occurs after a bond is broken. The particle-particle interaction force depends on the friction coefficient as well as the stiffness of these two particles. Therefore, collectively the material can sustain more compression and shear and this leads to an increase of the ultimate failure strength of the RVE. The friction and sliding free contact behaviour clearly emerges only in presence of compression, which explains why a better comparison of the strength is observed in Part-A. In fact, the post-failure friction and contact behaviour in compression and/or shear is closer to physical tests whilst the analytical methods usually cannot take it into account. However, Puck's criterion was among the theories that performed well for predicting the strength of unidirectional lamina subjected to transverse normal stress and in-plane shear as compared with experimental results [46]. In this study the criteria is further validated against our virtual modelling results for another type of biaxial loading scenario of transverse normal and transverse shear loading.

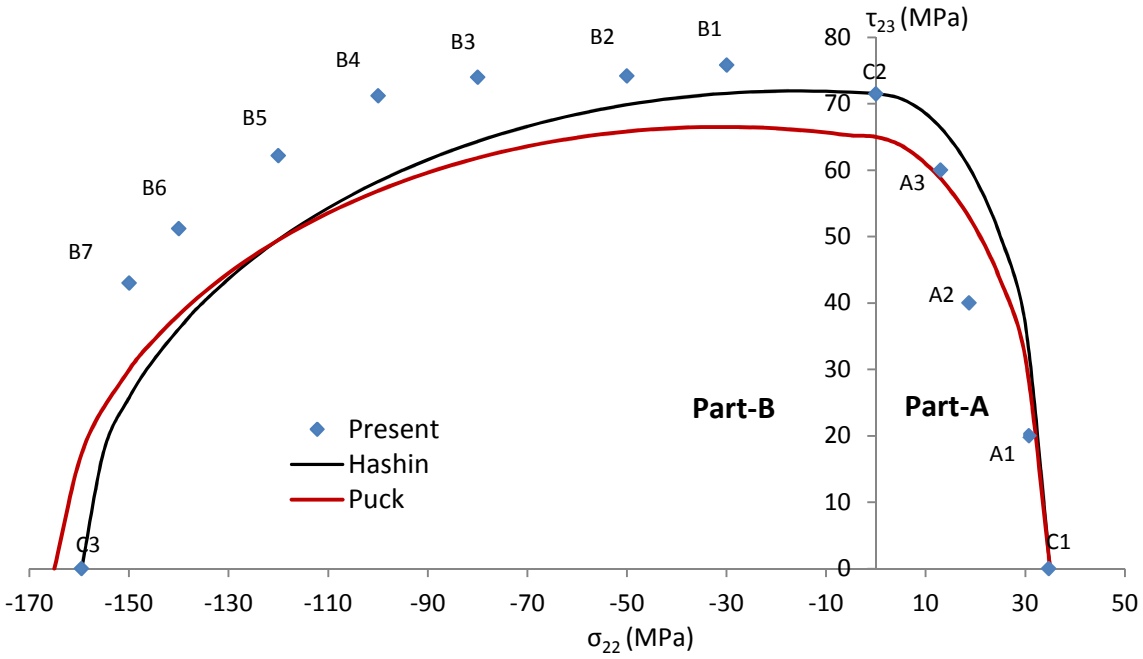

Fig.18 Failure envelope of a fibre-reinforced composite lamina in the σ_{22}-τ_{23} stress space.

5.2 DEM visualisation of damage evolution

In Puck's model failure under transverse normal and transverse shear depends on the orientation of failure plane which in turn depends on the magnitude of the normal and shear stresses acting on the failure plane surface. Thus, it is important to investigate the final failure planes of a RVE. The crack paths discussed in this section is for RVE #1 under different loading combinations (or τ_{23}/σ_{22} ratio) as shown in Fig.19. Each subfigure is associated with a loading combination along the failure envelope shown in Fig.18, such as C1, A1, A2, *etc*.

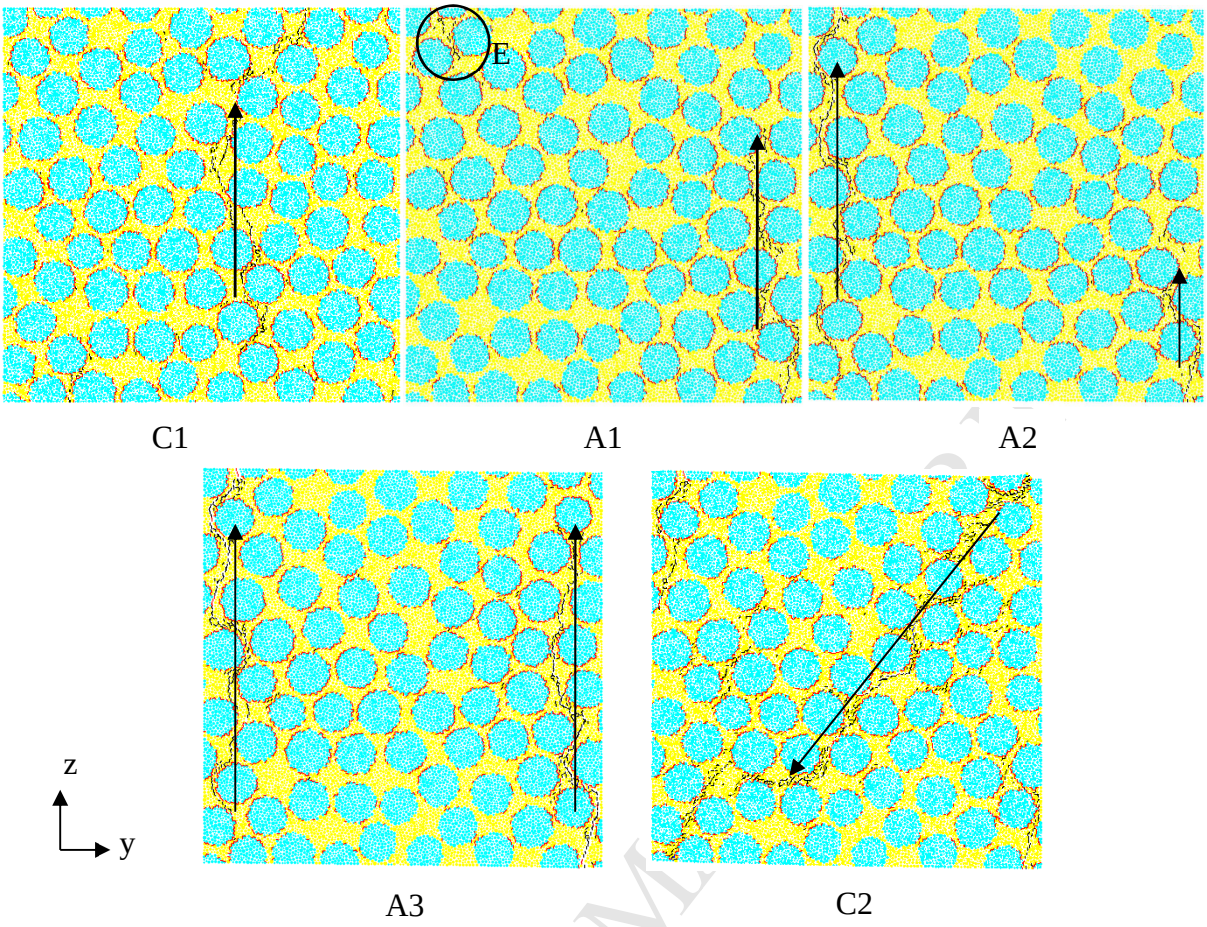

Fig.19 Accumulation of damages in the composite under different loading combinations in Part-A. (Each subfigure represents a data point on the failure envelope according to its label; Red dots represent fibre/matrix debonding and black dots represent matrix cracks.)

Fig.19C1, which is for the RVE under uniaxial transverse tension (point C1 in Fig.18), shows that the failure plane is found to be perpendicular to the loading axis and propagates between fibres in the middle of the RVE.

After applying transverse shear (*i.e.*, τ_{23}/σ_{22} = 2.1 at A1), the failure plane is still about 90° but not literally in the middle, and another failure path also appears as shown by the circle 'E' in Fig.19A1.

By increasing τ_{23}/σ_{22} ratio to 2.13 and 4.63, it has been found that the second failure path propagates longer in the RVE and eventually two vertical crack paths present, as shown in Fig.19A2 and A3.

Finally, the accumulated failure of the RVE subjected to pure transverse shear is plotted in Fig.19C2 where the plane angle is found to be around 45°, and the failure path is somehow diverted when fibres are present at the crack tip.

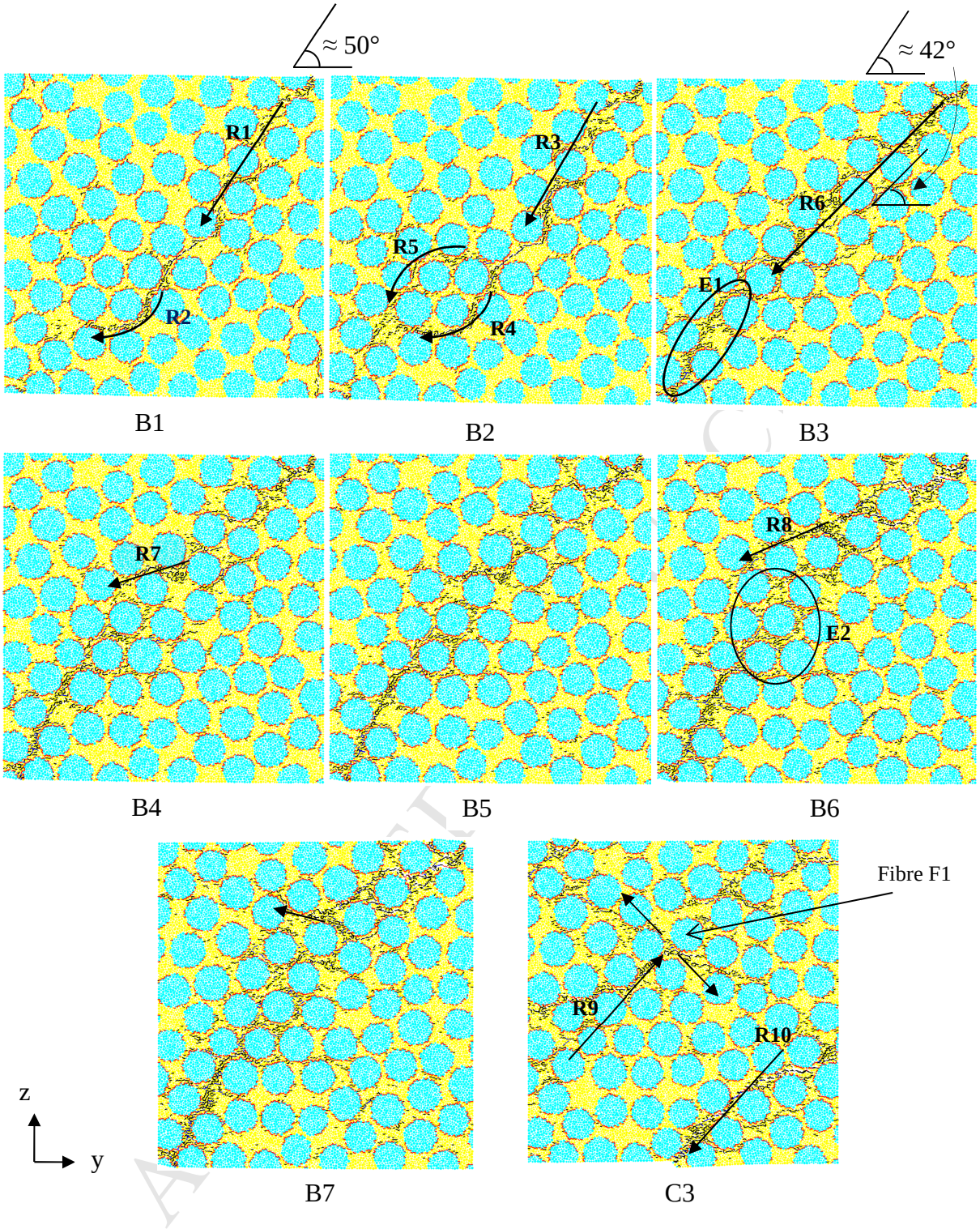

Fig.20 Accumulated cracks in the composite under different loading combinations. (Each subfigure represents a data point on the failure envelope according to its label; Red dots represent fibre/matrix debonding and black dots represent matrix cracks.)

The accumulated cracks in the composite subjected to combined transverse shear and transverse compression as well as pure transverse compression (Part-B of Fig.18) are shown

in Fig.20. Similar to what has been used above, each subfigure in Fig.20 is associated with one data point in Fig.18.

For low compression load (*i.e.* τ_{23}/σ_{22} = 2.5 or load case B1) in Fig.20B1, the critical failure plane is oriented at an angle of about 50° to the loading axis (*i.e.* y-axis), as indicated by the arrow R1. However, s fracture band cannot propagate through the fibres, the orientation alters slightly at the end and this variation is mainly caused by the fibre distribution, see arrow R2.

For smaller transverse shear and compression ratio, *i.e.*, point B2 in Fig.18, the initial fracture angle is almost the same as the previous case. However, another fracture band (which is sindicated by the arrow R5) appears and follows the first one, see Fig.20B2.

In Fig.20B3, the orientation angle of fracture plane is reduced more to become about 42° and also more cracks take place just before the final failure as indicated by the elliptic E1. According to Eq.(35), the fracture angle decreases when τ_{23}/σ_{22} is reduced, and this is confirmed by our DEM simulation results, *i.e.*, the fracture angle is reduced from 50° to 42° with increasing compression stress σ_{22}.

Failure patterns in Fig.20B4 and B5 are similar to that in Fig.20B3 except a new fracture path appears (indicated by the arrow R7) and has a small slope with y-axis.

Finally, it is found that with increasing transverse compression stress in Fig.20B6 and B7 more intensive cracks tend to occur between fibres which reduce the average fracture angle, In addition, more diverse crack paths appear (indicated by the arrow R8 in Fig.20B6) and the failure band becomes bigger than above cases.

The final failure of uniaxial compression stress is also included in and shown in the Fig. 20C3. The damage evolution of this loading case is similar to the one that has already been discussed in Section 4.2. As can be seen from Fig.20C3, two main failure paths, R9 and R10, are present. The crack path R8 runs through the RVE until it is constrained by fibre F1 and leads to new cracks occurring almost perpendicular to the initial path.

5.3 Quantitative analysis of damage events

A quantitative analysis of fibre/matrix debondings and matrix cracks is also carried out for each loading case in Part-A and Part-B of Fig.18, and the results are plotted in Fig.21 and Fig.22, respectively. Each column of the figure shows the number of interfacial debonding and matrix cracks of the corresponding loading case in Fig. 18. The matrix cracking includes both normal and shear breaking of bonds between the particles that represent the matrix. Columns labelled from A1 to A3 represent biaxial loads and are located in Part-A, whereas columns B1 to B7 are for those in Part-B and columns C1, C2 and C3 are for uniaxial transverse tension, shear and compression, respectively.

As shown in Fig.21 for the loading cases in Part-A, the number of fibre/matrix debondings is significantly high in the case of pure transverse tension (*i.e.*, column C1) and more matrix cracks are found in transverse shear, (i.e., column C2). While for combined transverse tension and shear, fibre/matrix and matrix cracks number increase steadily with increasing ratio of τ_{23}/σ_{22} from A1 to A3. It is important to mention that in all loading cases the fibre/matrix

interfacial debonding is the main damage mechanism before the peak stress as the bond strength of the fibre/matrix interface is much smaller than that of the matrix. While the matrix cracks mostly happen after the ultimate stress and leads to the final failure.

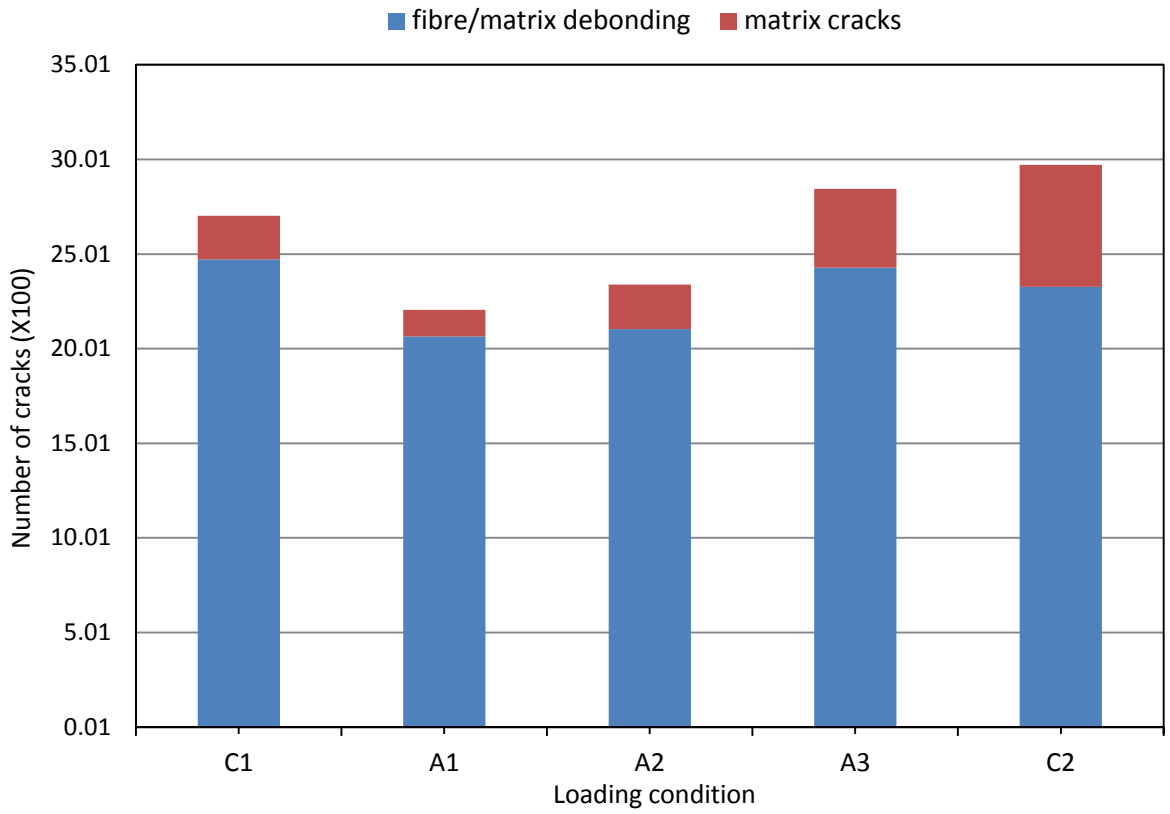

Fig.21 Number of fibre/matrix debonding and matrix cracks in loading cases in Part-A.

For Part-B of the failure envelope, it is found that the number of cracks in matrix has increased significantly with increasing compression loads from B1 to B6, as shown in Fig.22. Afterwards, the cracks number is almost the same as that in uniaxial compression loading case, C3. The number of fibre/matrix debonding also increases with load, but not as fast as matrix cracking. These results are reasonable as by increasing the confining compression load applied on the RVE in the first step (see Fig.17) would certainly leads to more cracks before the second step. In addition by increasing the initial stress in the bonds (that are not broken yet) before applying shear load on the RVE in the second step, would make them more susceptible to break in the subsequent shear load. High confining stress also increases strain softening which continues until the final failure, and thus more normal and shear cracks would occur. This explains the increase of the total number of damage events from B1 to B7 in Fig.22.

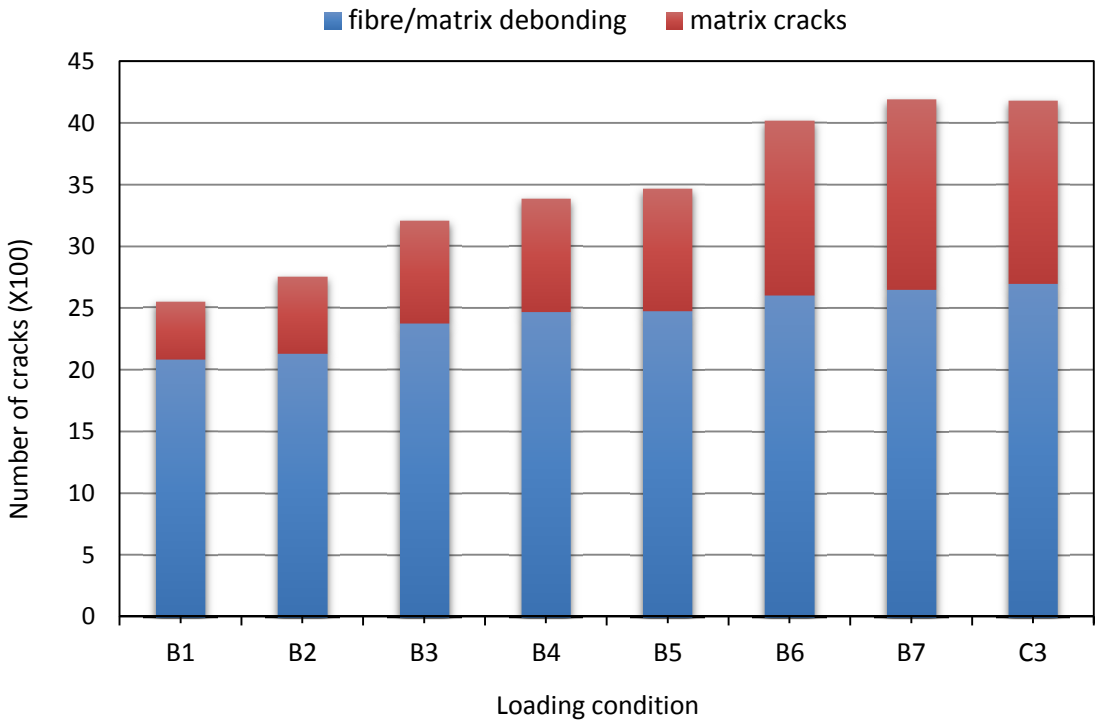

Fig.22 Number of fibre/matrix debonding and matrix cracks in loading cases in Part-B.

6. Conclusions

A 2D particle model based the discrete element method (DEM) has been developed to study the microscopic behaviour of unidirectional fibre reinforced composite laminae under different loading conditions. Calibration process is first carried out to relate micro parameters of the DEM models of fibre and matrix to macro properties of the materials. The critical size of RVE using DEM is investigated that a reasonable RVE size of $63\ \mu m \times 63\ \mu m$ can be used provided that the material constituents are previously calibrated. This method shows good prediction of the elastic modulus of composite materials as compared with FEM models using the same approach for generating random fibre distributions.

A micromechanical analysis is then carried out to investigate the microscopic failure mechanisms of a composite laminae of MY750 matrix reinforced by E-glass fibres under transverse compression and shear loading. The stress-strain curves are also produced for five different RVEs with different fibre distributions, from which compressive and shear strength has been obtained in together with the failure strains. It is found that DEM can better predict the stress-strain response of the composite under transverse compression than FEM as it clearly shows the compressive strength and compressive failure strain on the stress-strain curve. The shear strength has also been predicted. Previous FEM work, such as [19], shows more nonlinear behaviour of the stress-strain under transverse shear loads than DEM.

The DEM simulations have shown the microscopic failure mechanisms of the composite and the detailed damage evolution in the RVEs. For both transverse compression and shear loads, interfacial debonding occurs first and then matrix cracks become dominating in areas where

inter-fibre distances are small. Eventually, interfacial debonding and matrix cracks are merged together to form the catastrophic failure of the RVEs.

The failure envelope of the composite is computed from DEM simulations under transverse compression and transverse shear. The results presented in this study show that DEM can be used as a useful tool to predict the failure envelope of a general composite laminae subjected to complex biaxial combination of transverse normal and transverse shear loads. Although the results tend to be underestimated for transverse tension and shear whilst overestimated for transverse compression and shear when compared with Hashin and Puck failure criteria, they are still reasonable as the post failure mechanism in the DEM modelling is closer to that in real experimental tests. The capability of DEM to accurately predict the macroscopic response as well as microscopic failure mechanisms makes it a very useful tool to explore the effect of constituent properties on the behaviour of composite laminae. This is important from a material viewpoint to choose critical parameters to improve and optimize laminae stiffness as well as strength which are very difficult and expensive to obtain through experiments.

Extending the current 2D DEM model to 3D is essential in the future when modelling composite laminates under more complex triaxial loads where delamination as well as transverse cracking needs to be included. A fully developed 3D DEM model would be able to visualise the damage evolution and predict the failure envelope of composite laminates that are selected in the cases in WFEE-II. By doing so, it aims to identify the reasons for which the existing failure criteria are not accurate in certain loading cases and subsequently modify them or develop a new universal failure criterion that takes into account the damage progression for higher accuracy.

References

[1] Kaddour A, Hinton M. Maturity of 3D failure criteria for fibre-reinforced composites: Comparison between theories and experiments: Part B of WWFE-II. Journal of Composite materials. 2013;47(6-7):925-66.

[2] Hinton MJ, Kaddour AS, Soden PD. Failure criteria in fibre reinforced polymer composites: the world-wide failure exercise: Elsevier; 2004.

[3] Hashin Z. Failure criteria for unidirectional fiber composites. Journal of applied mechanics. 1980;47:329-34.

[4] Matzenmiller A, Lubliner J, Taylor R. A constitutive model for anisotropic damage in fiber-composites. Mechanics of Materials. 1995;20(2):125-52.

[5] Puck A, Schürmann H. Failure analysis of FRP laminates by means of physically based phenomenological models. Composites Science and Technology. 2002;62(12-13):1633-62.

[6] Davila CG, Camanho PP, Rose CA. Failure criteria for FRP laminates. Journal of Composite materials. 2005;39(4):323-45.

[7] González C, LLorca J. Mechanical behavior of unidirectional fiber-reinforced polymers under transverse compression: microscopic mechanisms and modeling. Composites Science and Technology. 2007;67(13):2795-806.

[8] Parıs F, Correa E, Cañas J. Micromechanical view of failure of the matrix in fibrous composite materials. Composites Science and Technology. 2003;63(7):1041-52.

[9] Ha SK, Jin KK, Huang Y. Micro-mechanics of failure (MMF) for continuous fiber reinforced composites. Journal of Composite materials. 2008.

[10] Trias D, Costa J, Turon A, Hurtado J. Determination of the critical size of a statistical representative volume element (SRVE) for carbon reinforced polymers. Acta materialia. 2006;54(13):3471-84.

[11] Yang L, Yan Y, Ma J, Liu B. Effects of inter-fiber spacing and thermal residual stress on transverse failure of fiber-reinforced polymer–matrix composites. Computational materials science. 2013;68:255-62.

[12] Sheng Y, Yang D, Tan Y, Ye J. Microstructure effects on transverse cracking in composite laminae by DEM. Composites Science and Technology. 2010;70(14):2093-101.

[13] Ismail Y, Sheng Y, Yang D, Ye J. Discrete element modelling of unidirectional fibre-reinforced polymers under transverse tension. Composites Part B: Engineering. 2015;73:118-25.

[14] Yang D, Ye J, Tan Y, Sheng Y. Modeling progressive delamination of laminated composites by discrete element method. Computational materials science. 2011;50(3):858-64.

[15] Yang D, Sheng Y, Ye J, Tan Y. Dynamic simulation of crack initiation and propagation in cross-ply laminates by DEM. Composites Science and Technology. 2011.

[16] Maheo L, Dau F, Andre D, Charles J-L, Iordanoff I. A promising way to model cracks in composite using Discrete Element Method. Composites Part B: Engineering. 2015;71:193-202.

[17] Canal LP, Segurado J, LLorca J. Failure surface of epoxy-modified fiber-reinforced composites under transverse tension and out-of-plane shear. International journal of solids and structures. 2009;46(11):2265-74.

[18] O'Dwyer D, O'Dowd N, McCarthy C. Investigation of strain hardening effects under in-plane shear of unidirectional composite materials. Computational materials science. 2012;64:179-82.

[19] Romanowicz M. Determination of the first ply failure load for a cross ply laminate subjected to uniaxial tension through computational micromechanics. International journal of solids and structures. 2014;51(13):2549-56.

[20] Totry E, González C, LLorca J. Failure locus of fiber-reinforced composites under transverse compression and out-of-plane shear. Composites Science and Technology. 2008;68(3):829-39.

[21] Totry E, Molina-Aldareguía JM, González C, LLorca J. Effect of fiber, matrix and interface properties on the in-plane shear deformation of carbon-fiber reinforced composites. Composites Science and Technology. 2010;70(6):970-80.

[22] Vaughan T, McCarthy C. A micromechanical study on the effect of intra-ply properties on transverse shear fracture in fibre reinforced composites. Composites Part A: Applied Science and Manufacturing. 2011;42(9):1217-28.

[23] André D, Iordanoff I, Charles J-l, Néauport J. Discrete element method to simulate continuous material by using the cohesive beam model. Computer Methods in Applied Mechanics and Engineering. 2012;213:113-25.

[24] Potyondy D, Cundall P. A bonded-particle model for rock. International journal of rock mechanics and mining sciences. 2004;41(8):1329-64.

[25] Itasca. PFC2D-particle Flow Code (Itasca Consulting Group Inc., Minnesta). 2003.

[26] Lubachevsky BD, Stillinger FH. Geometric properties of random disk packings. Journal of statistical Physics. 1990;60(5-6):561-83.

[27] Sherwood J. Packing of spheroids in three-dimensional space by random sequential addition. Journal of Physics A: Mathematical and General. 1997;30(24):L839.

[28] Weitz DA. Packing in the spheres. Science. 2004;303(5660):968-9.

[29] Boutt D, McPherson B. The role of particle packing in modeling rock mechanical behavior using discrete elements. Geotechnical Special Publication. 2002:86-92.

[30] Nguyen N-S, Magoariec H, Cambou B, Danescu A. Analysis of structure and strain at the meso-scale in 2D granular materials. International journal of solids and structures. 2009;46(17):3257-71.

[31] Yan G, Yu H-s, McDowell G. Simulation of granular material behaviour using DEM. Procedia Earth and Planetary Science. 2009;1(1):598-605.

[32] Cho Na, Martin C, Sego D. A clumped particle model for rock. International journal of rock mechanics and mining sciences. 2007;44(7):997-1010.

[33] Soden P, Hinton M, Kaddour A. Lamina properties, lay-up configurations and loading conditions for a range of fibre-reinforced composite laminates. Composites Science and Technology. 1998;58(7):1011-22.

[34] Ugural AC, Fenster SK. Advanced strength and applied elasticity: Pearson education; 2003.

[35] Ogihara S, Koyanagi J. Investigation of combined stress state failure criterion for glass fiber/epoxy interface by the cruciform specimen method. Composites Science and Technology. 2010;70(1):143-50.

[36] Wang Y, Tonon F. Calibration of a discrete element model for intact rock up to its peak strength. International journal for numerical and analytical methods in geomechanics. 2010;34(5):447-69.

[37] Ismail Y, Yang D, Ye J. Discrete element method for generating random fibre distributions in micromechanical models of fibre reinforced composite laminates. Composites Part B: Engineering http://dxdoiorg/101016/jcompositesb201601037. 2016.

[38] Wongsto A, Li S. Micromechanical FE analysis of UD fibre-reinforced composites with fibres distributed at random over the transverse cross-section. Composites Part A: Applied Science and Manufacturing. 2005;36(9):1246-66.

[39] Vaughan T, McCarthy C. Micromechanical modelling of the transverse damage behaviour in fibre reinforced composites. Composites Science and Technology. 2011;71(3):388-96.

[40] Yang L, Yan Y, Liu Y, Ran Z. Microscopic failure mechanisms of fiber-reinforced polymer composites under transverse tension and compression. Composites Science and Technology. 2012;72(15):1818-25.

[41] Yang L, Wu Z, Cao Y, Yan Y. Micromechanical modelling and simulation of unidirectional fibre-reinforced composite under shear loading. Journal of Reinforced Plastics and Composites. 2015;34(1):72-83.

[42] Soden P, Hinton M, Kaddour A. A comparison of the predictive capabilities of current failure theories for composite laminates. Composites Science and Technology. 1998;58(7):1225-54.

[43] Vogler T, Kyriakides S. Inelastic behavior of an AS4/PEEK composite under combined transverse compression and shear. Part I: experiments. International Journal of Plasticity. 1999;15(8):783-806.

[44] Hsu S-Y, Vogler T, Kyriakides S. Inelastic behavior of an AS4/PEEK composite under combined transverse compressionand shear. Part II: modeling. International Journal of Plasticity. 1999;15(8):807-36.

[45] Totry E, González C, LLorca J. Influence of the loading path on the strength of fiber-reinforced composites subjected to transverse compression and shear. International journal of solids and structures. 2008;45(6):1663-75.

[46] Soden P, Kaddour A, Hinton M. Recommendations for designers and researchers resulting from the world-wide failure exercise. Composites Science and Technology. 2004;64(3):589-604.